Research Square

Preprints are preliminary reports that have not undergone peer review.
They should not be considered conclusive, used to inform clinical practice,
or referenced by the media as validated information.

Bridging dental and skeletal biology: dental tissue-derived mesenchymal stromal cells as models for studying physiological osteogenesis

Bibiána Baďurová
Comenius University in Bratislava, Jessenius Faculty of Medicine in Martin
Romana Záhumenská
Comenius University in Bratislava, Jessenius Faculty of Medicine in Martin
Tereza Pavlišová
Comenius University in Bratislava, Jessenius Faculty of Medicine in Martin
Bronislava Gašperová
Comenius University in Bratislava, Jessenius Faculty of Medicine in Martin
Veronika Kucháriková
Comenius University in Bratislava, Jessenius Faculty of Medicine in Martin
Dana Dvorská
Comenius University in Bratislava, Jessenius Faculty of Medicine in Martin
Lucia Kotúľová
Comenius University in Bratislava, Jessenius Faculty of Medicine in Martin
Nela Žideková
Comenius University in Bratislava, Jessenius Faculty of Medicine in Martin
Martin Kertys
Comenius University in Bratislava, Jessenius Faculty of Medicine in Martin
Sarah Kalmanová
Comenius University in Bratislava, University Hospital in Martin and Jessenius Faculty of Medicine in Martin
Rastislav Juríček
Comenius University in Bratislava, University Hospital in Martin and Jessenius Faculty of Medicine in Martin
Mária Janíčková
Comenius University in Bratislava, University Hospital in Martin and Jessenius Faculty of Medicine in Martin
Mária Kovalská
Comenius University in Bratislava, Jessenius Faculty of Medicine in Martin
Ján Strnádel
Comenius University in Bratislava, Jessenius Faculty of Medicine in Martin

Zuzana Hatoková
Comenius University in Bratislava, Jessenius Faculty of Medicine in Martin
Slavomíra Nováková
Comenius University in Bratislava, Jessenius Faculty of Medicine in Martin
Erika Halašová
Comenius University in Bratislava, Jessenius Faculty of Medicine in Martin
Henrieta Škovierová
henrieta.skovierova@uniba.sk

Comenius University in Bratislava, Jessenius Faculty of Medicine in Martin

---

Research Article

Keywords: Dental tissue-derived mesenchymal stromal cells, Osteoblasts, Osteogenic differentiation, Bone regeneration

Posted Date: September 25th, 2026

DOI: https://doi.org/10.21203/rs.3.rs-10447323/v1

License: This work is licensed under a Creative Commons Attribution 4.0 International License.
Read Full License

Additional Declarations: No competing interests reported.

Bridging dental and skeletal biology: dental tissue-derived mesenchymal stromal cells as models for studying physiological osteogenesis

Bibiána Baďurová[1], Romana Záhumenská[1,#], Tereza Pavlišová[1], Bronislava Gašperová[1,2], Veronika Kucháriková[1,2], Dana Dvorská[1], Lucia Kotúľová[1], Nela Žideková[1], Martin Kertys[3], Sarah Kalmanová[4], Rastislav Juríček[4], Mária Janíčková[4], Mária Kovalská[5], Ján Strnádel[1], Zuzana Hatoková[1], Slavomíra Nováková[1], Erika Halašová[1], Henrieta Škovierová[1*]

1 Comenius University in Bratislava, Jessenius Faculty of Medicine in Martin, Biomedical Centre Martin, Martin, Slovak Republic

2 Comenius University in Bratislava, Jessenius Faculty of Medicine in Martin, Department of Medical Biochemistry, Martin, Slovak Republic

3 Comenius University in Bratislava, Jessenius Faculty of Medicine in Martin, Department of Pharmacology, Martin, Slovak Republic

4 Comenius University in Bratislava, University Hospital in Martin and Jessenius Faculty of Medicine in Martin, Department of Stomatology and Maxillofacial Surgery, Martin, Slovak Republic

5 Comenius University in Bratislava, Jessenius Faculty of Medicine in Martin, Department of Histology and Embryology, Martin, Slovak Republic

Present address: Comenius University in Bratislava, Jessenius Faculty of Medicine in Martin, Biobank for Cancer and Rare Diseases, Martin, Slovak Republic

* Corresponding Author; e-mail: henrieta.skovierova@uniba.sk

Abstract

Background Dental tissue-derived mesenchymal stromal cells (DSCs) represent an accessible and minimally invasive cell source for bone regenerative applications. However, the extent to which they recapitulate the molecular and functional characteristics of human bone cells in physiologically relevant *in vitro* models of osteogenic differentiation remains incompletely understood. Therefore, we performed a comprehensive comparative analysis of osteogenic commitment in DSCs and normal human osteoblasts (NHOst).

Methods Mesenchymal stromal cells isolated from adult dental pulp (DPSCs) as well as from exfoliated deciduous teeth (SHEDs), and NHOst were cultured under osteogenic conditions and analyzed at early and late stages using complementary phenotypic, transcriptomic, protein and metabolomic approaches, including mineralization assays, RT2 Profiler PCR Arrays, immunocytochemistry and targeted metabolomics.

Results All three cell populations successfully acquired an osteogenic phenotype, accompanied by extracellular matrix mineralization, reduced proliferative activity and characteristic morphological changes. Comparative transcriptomic and protein analyses identified a shared molecular response involving extracellular matrix organization and bone-related signaling, with *CSF3, ICAM1,* and *MMP8* among the most consistently upregulated genes. Targeted metabolomic profiling further revealed extensive metabolic reprogramming involving amino acid, lipid and energy metabolism. Kynurenine emerged as the most prominent differentiation-associated metabolite detected across the DSCs and NHOst populations.

Conclusions We demonstrated that DSCs acquire an osteoblast-like profile that closely resembles primary NHOst while retaining selected cell type-specific characteristics. These findings support the potential of DSCs as a biologically relevant *in vitro* model for investigating osteogenesis and as a valuable experimental platform for bone biology, regenerative medicine, and hard tissue engineering.

Keywords Dental tissue-derived mesenchymal stromal cells, Osteoblasts, Osteogenic differentiation, Bone regeneration

Background

Bone is a highly specialized tissue that provides structural support, enables locomotion, protects vital organs, and serves as a dynamic reservoir for mineral homeostasis. Although bone possesses an intrinsic capacity for regeneration, its self-repair potential is generally limited to small defects and is often insufficient to restore extensive bone loss resulting from trauma, congenital abnormalities, tumor resection, or degenerative diseases [1]. Current treatment strategies, including autologous and allogeneic bone grafting, remain associated with important limitations such as donor site morbidity, limited tissue availability, and the risk of graft failure. Consequently, the development of advanced bone tissue engineering (BTE) approaches has become a major focus of regenerative medicine (RM), with particular emphasis on stem cell-based therapies.

Dental tissue-derived mesenchymal stromal cells (DSCs) represent an attractive source of mesenchymal stromal cells (MSCs) owing to their accessibility, minimally invasive procurement, and fewer ethical concerns than many other stem cell sources. In addition, they exhibit high proliferative capacity, multilineage differentiation potential, trophic activity, and immunomodulatory properties. Their therapeutic applicability extends well beyond the oral cavity, encompassing not only dental and craniofacial tissues but also bone, neural, vascular, and other extraoral tissues [2-5]. A particularly well-characterized and extensively studied DSCs population is represented by dental pulp-derived MSCs. These cells can be isolated from both adult teeth (DPSCs) and exfoliated deciduous teeth (SHEDs), with SHEDs generally demonstrating greater proliferative capacity and enhanced stemness characteristics compared with DPSCs [6]. Nevertheless, both cell populations exhibit strong osteogenic differentiation potential and have been investigated as promising candidates for cell-based therapies and BTE applications [7]. Osteogenic differentiation of MSCs is a tightly regulated multilevel process governed by the sequential activation of lineage-specific transcription factors, signaling pathways, and

biochemical/biomechanical stimuli provided by the extracellular matrix (ECM). Key regulators include RUNX2, DLX5, and OSX, which coordinate the transition from proliferating progenitors to ECM-producing osteoblasts and ultimately to mature bone-forming cells. This process is accompanied by dynamic changes in the expression mostly of osteogenic markers, including ALP, BSP, COL1A1, OCN, OPN, and PHEX reflecting progressive commitment, ECM maturation, and mineralization [8,9]. Beyond its structural role, the ECM also regulates cell behavior through mechanical and biochemical cues, earning it the title of the "fourth element" in TE [10]. Osteoblasts secrete the matrix and initiate mineralization of the osteoid, requiring a surface scaffold (predominantly collagens) to synthesize new ECM. Interestingly, the structural form of collagens influences osteoblast behavior: while fibrillar forms support cell proliferation, denatured forms may suppress proliferation, but enhance osteogenic differentiation. Thus, collagens serve both as a physical scaffold and as a biological modulator of osteoblast function, proliferation, and maturation [10,11]. Moreover, increasing evidence indicates that osteogenesis is closely linked to extensive cellular remodeling involving not only transcriptional regulation and ECM production but also metabolic adaptation required to support ECM synthesis, mineralization, and cell differentiation.

A number of studies have demonstrated the osteogenic potential of DSCs. However, the extent to which developmentally distinct DSCs populations recapitulate the osteogenic characteristics of primary normal human osteoblasts (NHOst) remains incompletely characterized, particularly at the integrated phenotypic, molecular, and metabolic levels. In biomedical research, NHOst cells represent a widely used non-transformed *in vitro* model for investigating bone development, ECM mineralization, and cellular responses to biomaterials and implant surfaces [12,13]. In contrast to commonly used osteosarcoma-derived cell lines, which often display altered proliferative and differentiation behavior, NHOst cells provide a physiologically relevant reference for human osteogenic studies. Moreover, integrated studies capturing the osteogenic dynamics between these populations remain limited.

In this study, we comprehensively compared osteogenic differentiation of DPSCs, SHEDs, and NHOst across phenotypic, functional, transcriptional, protein, and metabolic levels to characterize common and cell type-associated features of the differentiation process. To our knowledge, this is the first study to provide an integrated multi-level comparison of osteogenic differentiation between DSCs and NHOst. The obtained results advance our understanding of the biological relationship between these populations and further support the use of DSCs as accessible cellular models for studies of osteogenesis, providing a foundation for future research in BTE and regenerative therapies.

Materials and methods

Monitoring of cell morphology

The morphology of the control (CM) and osteogenically induced (OM) cells was monitored throughout the experiment. Bright-field photomicrographs were captured by a light microscope (Optika IM-3, Ponteranica, Italy) on Day 1 (D1), Day 5 (D5), Day 10 (D10), and Day 15 (D15) after the beginning of osteogenic differentiation.

Isolation, expansion, and osteogenic differentiation of cells

Three cell populations were investigated: DPSCs, SHEDs, and NHOst cells, with one donor-derived preparation representing each cell type (n = 1 donor per cell type). The three populations were analyzed independently; therefore, observed similarities or differences were interpreted as findings specific to the respective populations rather than as population-level effects in multiple donors. Human DPSCs and SHEDs were isolated according to our optimized protocol [14]. All *in vitro* cell experiments were approved by the Ethical Committee of the Jessenius Faculty of Medicine, Comenius University (approval No. EK 24/2020; date of approval 18 April 2020). Cells from donor 1 (DPSCs; 27-years old female) and donor 2 (SHEDs; 7-years old male) were obtained from the Department of Stomatology and Maxillofacial Surgery, University Hospital Martin. Donor 3 (NHOst; 33-years old male) was purchased from Lonza (Basel, Switzerland; Ref. CC-2538; Lot 19TL092044). DPSCs and SHEDs were

grown in DMEM/F-12, GlutaMAX™ (Gibco, Thermo Fisher Scientific, Waltham, MA, USA) culture medium supplemented with 10% FBS (Gibco) and 100 U/mL penicillin and 100 µg/mL streptomycin (Biosera, Nuaille, France). Commercially available NHOst was grown in OBM culture medium supplemented with 10% FBS, 1% ascorbic acid, 30 µg/mL gentamycin sulfate, and 15 ng/mL amphotericin B (Lonza). All cells were grown in standard culture conditions (5% CO_2, 37 °C, humidified conditions) and seeded at a density of 5 × 10^3 cells/cm^2. When cells reached 60% confluence, they were differentiated using the commercially available osteogenic differentiation medium OsteoMAX-XF™ (Merck, Darmstadt, Germany) supplemented with 100 U/mL penicillin and 100 µg/mL streptomycin (Biosera). Unexposed controls were prepared simultaneously. Culture medium was replaced every 3rd day. Cells were analyzed at an early (D5) and a late (D15) stage of osteogenic differentiation using the individual analytical approaches described below, which were performed on passages 3-5 (Fig. 1).

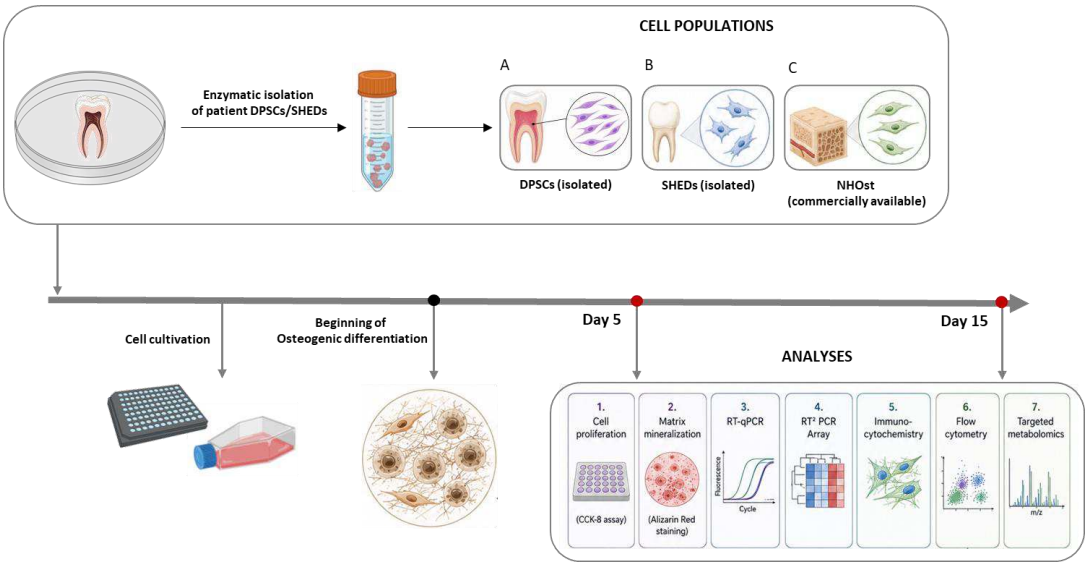


Fig. 1 Schematic overview of the experimental workflow. DPSCs, SHEDs, and NHOst cells, each represented by a single donor-derived cell population underwent osteogenic differentiation and were analyzed at early (Day 5) and late (Day 15) stages using complementary phenotypic, molecular, protein, and metabolic approaches.

Alizarin Red S staining and calcium deposit quantification

Analysis was evaluated on D5 and D15 based on our optimized protocol [15]. Briefly, CM and OM were washed with DPBS, followed by fixation in 4% PFA (v/v) (Cell Signaling Technology, Danvers, MA, USA)

for 30 min in the dark at RT. After washing with DPBS, 2% Alizarin Red S (Merck) was added for 3 min. The dye was removed, and the stained deposits were carefully washed with ddH_2O and visualized using a light microscope (Optika IM-3). Then, the calcium deposits were destained (10% acetic acid (v/v) + 20% methanol (v/v)) and centrifuged at 9,500 × g, 15 °C for 10 min. Subsequently, the absorbance of individual samples was read at a wavelength of 405 nm using an Epoch microplate reader (BioTek Instruments, Winooski, VT, USA). The results were normalized to the total amount of protein. The protein concentration was determined by the BCA assay (Pierce Biotechnology, Thermo Fisher Scientific, Rockford, IL, USA).

Flow cytometry

The expression of CD9, CD44, CD45, CD73, CD90, and CD105 markers was analyzed by flow cytometry on D5 and D15. Single-cell suspension of CM and OM was prepared and centrifuged at 450 × g at 13 °C for 4 min, and cells were resuspended in FACS buffer (5% (v/v) mouse serum in DPBS, 1 mmol/L EDTA). After blocking for 30 min in the dark on ice, CD markers (BioLegend, San Diego, CA, USA) were incubated with cell samples for 60 min in the dark on ice. Consequently, labeled samples were washed with DPBS followed by centrifugation at 450 × g, 13 °C for 4 min, and the pellet was resuspended in FACS buffer. A single measurement was performed for each sample. The samples were analyzed by BD FACS Diva software (v8.0.1) on a flow cytometer (BD Biosciences FACS Aria, San Jose, CA, USA). Analysis was performed on 10,000 events and gating was set up using an unstained/isotype control. Gating was applied uniformly and dead cells as well as debris were excluded from the analysis across all samples at each time point. In addition to the percentage of positive CD marker expression, the mean fluorescence intensity (MFI) was determined for the positively gated cell population of each marker using the same gating strategy.

Cell proliferation assay

Proliferation of CM and OM was evaluated on D1, D5, D10, and D15 using the Cell Counting Kit-8 (CCK-8; Sigma-Aldrich) according to the manufacturer's protocol. At each time point, the CCK-8 reagent was added to the culture medium at 10% (v/v). The cells were then incubated for 5 h under standard culture conditions (37 °C, 5% CO_2). After incubation, the plate was gently shaken, and absorbance was measured at a wavelength of 450 nm with background correction at 650 nm using an Epoch microplate reader (BioTek).

RNA isolation and quality determination

Total RNA was isolated from CM and OM on D5 and D15 using the NucleoSpin® RNA Plus Kit (Macherey-Nagel GmbH & Co. KG, Düren, Germany) according to the manufacturer's instructions. Briefly, lysis buffer was added to the cell pellet, and lysate was loaded onto the column followed by centrifugation at 11,000 × g for 30 s. The binding solution was added to the flow-through, and the mixture was applied to the column, followed by centrifugation. The bound RNA was washed with Wash Buffer 1, twice with Wash Buffer 2 and centrifuged at 11,000 × g for 15 s. RNA was eluted with RNase-free water. RNA concentration and purity were determined spectrophotometrically using a NanoDrop™ One instrument (Thermo Fisher Scientific). The quality and integrity of the isolated RNA were assessed by Agilent 2100 Bioanalyzer using RNA 6000 Nano Kit (Agilent Technologies, Santa Clara, CA, USA). Only samples exhibiting RNA Integrity Number (RIN) greater than 9.5 were used for subsequent analyses.

RT2 PCR Array-based osteogenic gene profiling

To investigate transcriptional differences between CM and OM, RNA isolated from samples collected at D5 and D15 was analyzed using the RT2 Profiler™ PCR Array Human Osteogenesis (PAHS-026ZA, QIAGEN GmbH), according to the manufacturer's instructions. The array enables simultaneous analysis of 84 genes associated with osteogenic differentiation, including those involved in skeletal development, bone mineral metabolism, ECM organization, and cell adhesion. Total RNA (1 µg) was treated with genomic DNA elimination buffer (42 °C, 5 min), followed by reverse transcription (42 °C

for 15 min) to generate cDNA using RT2 First Strand Kit (QIAGEN GmbH, Hilden, Germany) as recommended by the manufacturer. The resulting cDNA was combined with RT2 SYBR Green MasterMix, RNase-free water, and the reaction mixture (25 µL) and was loaded into the array plate. Real-time PCR amplification was performed using a QuantStudio™ 7 Real-Time PCR System (Applied Biosystems, Thermo Fisher Scientific, Foster City, CA, USA). The array included five housekeeping genes (*β-actin, β-2-microglobulin, glyceraldehyde-3-phosphate dehydrogenase, hypoxanthine phosphoribosyl- transferase 1, ribosomal protein lateral stalk subunit P0; ACTB, B2M, GAPDH, HPRT1, RPLP0*) for normalization, along with internal controls for gDNA contamination, reverse transcription efficiency, and PCR performance. Raw Ct values were analyzed using the GeneGlobe Data Analysis Center (QIAGEN GmbH; https://geneglobe.qiagen.com/sk/analyze; accessed on 29 May 2024). Gene expression was normalized to the geometric mean of the most stable reference genes selected by the software, and relative expression levels were calculated using the 2^−ΔΔCt method. Differential gene expression was determined by comparing OM samples with time-matched CM samples (D5 as well as D15). Changes between time points were also evaluated to assess transcriptional dynamics during osteogenic differentiation. Genes with log2 fold change |log2FC| ≥ 1 were considered differentially expressed. Heatmaps, scatter plots, and FC values were generated using GeneGlobe. Based on these results, ten differentially expressed genes were selected for validation by RT-qPCR using a custom RT2 Profiler™ PCR Array plate (QIAGEN GmbH). For validation, cDNA was prepared as described above and amplified using RT2 SYBR Green Mastermix on a QuantStudio™ 7 Real-Time PCR System. Gene expression was normalized to the most stable housekeeping genes (*GAPDH, HPRT1*, and *RPLP0)*.

Immunocytochemistry

Immunocytochemical staining was evaluated on D5 and D15. Cells grown in dark 96-well plates (Sarstedt AG & Co. KG, Nümbrecht, Germany) were washed with DPBS and fixed in 4% PFA (v/v) (Cell Signaling Technology) for 30 min in the dark at RT. After washing, cells were incubated with specific antibodies. Samples stained with Alexa Fluor® 488 Phalloidin (Abcam, Cambridge, UK, ab176753,

1:1,000 in a solution of 1% BSA (w/v) in DPBS) were incubated for 60 min. Consequently, the samples were labeled with 1 µg/mL DAPI dye (Sigma-Aldrich) for 10 min in the dark at RT. The cells were washed with DPBS and analyzed by fluorescence microscope (WiScan®, Hermes IDEA Bio-Medical, Rehovot, Israel). Samples stained with specific primary antibodies APOA2 (Abcam, Cambridge, UK, ab92478, rabbit, 1:200), BSP2 (Sigma-Aldrich, MAB1061, mouse, 1:100), COL1A1 (Cell Signaling Technology, 39952, rabbit, 1:500), DMP1 (Invitrogen, Thermo Fisher Scientific, Carlsbad, CA, USA, PA5-103323, rabbit, 1:500), DSPP (Invitrogen, PA5-76382, rabbit, 1:200), OPN (Sigma-Aldrich, HPA027541, rabbit, 1:100) were washed with DPBS and incubated in blocking solution (5% (v/v) goat serum + 0.2% (v/v) Triton X-100 in DPBS) for 60 min in the dark at RT. The samples were incubated with primary antibodies in a blocking solution overnight at 4 °C. After washing with DPBS, the fluorescent secondary antibody (Abcam, ab150077, antirabbit, 1:500; Abcam, ab150113, antimouse, 1:500) in a blocking solution was added for 60 min in the dark at RT. Consequently, the samples were labeled with 1 µg/mL DAPI dye (Sigma-Aldrich) for 10 min in the dark at RT. Cells were washed with DPBS and analyzed by fluorescence microscope (WiScan®). Negative controls were included for all samples, where cells were stained exclusively with the fluorescent secondary antibody, omitting the primary antibodies to confirm the absence of autofluorescence of the cells. Semiquantitative image analysis was performed using Fiji/ImageJ software (v1.8.0_345) [16] according to a previously established protocol [14]. Briefly, individual fluorescence channels were separated and analyzed independently. Cell nuclei were quantified from DAPI-stained images using a fixed threshold applied uniformly across all samples. The fluorescence signal corresponding to the target protein was then quantified using identical threshold settings for all samples stained with the same antibody at a given time point. To minimize the influence of variations in cell number, fluorescence intensity values were normalized to the corresponding nucleus count and subsequently expressed relative to the appropriate control group.

Metabolite profiling and quantification

Samples from CM and OM cultures were collected at D5 and D15. Intracellular metabolites were extracted by isopropanol precipitation to rapidly quench cellular metabolism and preserve labile intermediates. Briefly, cells were washed with ice-cold physiological saline (0.9% NaCl) and lysed directly in culture flasks using ice cold 100% isopropanol (-20 °C). Extracts were vortexed for 30 s, and sonicated in an ice-cold water bath (3 × 30 s). Protein precipitation was performed by incubation at -20 °C for 60 min, followed by centrifugation at 16,000 × g for 20 min at 4 °C. Supernatants containing metabolites were collected and stored at -80 °C until analysis. For protein quantification, the residual pellet was resuspended in SDT buffer [17], vortexed for 1 min, and incubated at 20 °C for 2 h on a shaker (1200 rpm). Samples were then centrifuged at 14,000 × g for 20 min at 20 °C, and protein extracts were collected and stored at -80 °C. Targeted metabolomic profiling was performed using the AbsoluteIDQ® p180 kit (Biocrates Life Sciences AG, Innsbruck, Austria), enabling the simultaneous quantification of 185 metabolites, including acylcarnitines, amino acids, biogenic amines, ether-linked phosphatidylcholines, phosphatidylcholines, lysophosphatidylcholines, sphingomyelins, and hexoses. Intracellular metabolites obtained from DPSCs, SHEDs, and NHOst cells and appropriate extracellular metabolites were analyzed. A single measurement was performed for each sample. Metabolite quantification and data processing were performed using MassLynx v4.2 (Waters, Prague, Czech Republic) and WebIDQ software (Biocrates). Quality control procedures followed the manufacturer's recommendations. Metabolites showing a coefficient of variation >25% in QC samples or with >50% of values below the limit of detection (LOD) or limit of quantification (LOQ) were excluded from further analysis [18-20]. Intracellular metabolite abundances were normalized to total protein determined using the Pierce™ 660 nm Protein Assay Kit (Pierce Biotechnology) according to the manufacturer's instructions. Extracellular metabolite abundances were corrected by subtracting the background values measured in the corresponding cell-free culture medium. Intracellular and extracellular metabolite abundances were expressed as the OM/CM log2FC ratio, whereas temporal metabolic changes in OM were expressed as the D15/D5 log2FC ratio. Positive log2FC ratios indicate increased metabolite abundance, whereas negative log2FC ratios indicate decreased metabolite abundance.

Interpretation focused on metabolites exhibiting substantial changes (|log2FC| ≥ 1) for each cell type and time point. Results were visualized using boxplots.

Statistical analysis

All statistical analyses and visualizations were performed in R (v4.5.3), using packages including ggplot2 (v4.0.2) and ggpubr (v0.6.3) [21-23]. Each cell type was represented by a single donor-derived culture (biological n = 1 per cell type), with replicate measurements within each experiment representing technical replicates. Accordingly, *p*-values derived from technical measurements were used as exploratory/descriptive statistical comparisons of the observed measurements and were not interpreted as evidence of biological statistical significance or population-level inference. For cell proliferation, four technical measurements were obtained for each condition and time point and summarized as mean ± standard deviation (SD). Comparisons between OM and CM were evaluated using *p*-values derived from these technical measurements. Mineralization was assessed using three technical replicates per condition and time point and summarized as mean ± SD, with OM/CM comparisons evaluated in the same manner. For transcriptional profiling, gene expression changes were expressed as log2FC, and genes meeting the predefined threshold of |log2FC| ≥ 1 were considered for further analysis. Results were visualized using bar plots and Venn diagrams. RT-qPCR verification was performed using three technical measurements for each gene, which were averaged prior to relative expression analysis using the 2^-ΔΔCt method. The resulting FC values were visualized using heatmaps and evaluated based on the magnitude and direction of change and concordance with the RT2 Profiler™ PCR Array findings. Protein expression assessed by immunocytochemistry was based on three technical replicates, with data presented as mean ± SD and OM/CM comparisons evaluated using *p*-values derived from the technical measurements.

Results

Transition from proliferation to osteogenic maturation

Morphological assessment revealed progressive changes associated with osteogenic differentiation in all three cell types throughout the 15-day differentiation period (Fig. S1). All CM populations displayed stable growth and retained their characteristic morphology; a spindle-shaped mesenchymal appearance in DPSCs and SHEDs, and an elongated shape in NHOst. In contrast, all OM types underwent progressive morphological remodeling accompanied by ECM deposit production and mineralized nodule formation. DPSCs exhibited the earliest detectable morphological alterations, whereas similar changes in SHEDs and NHOst became evident during the subsequent stages of differentiation. Notably, differentiated NHOst cultures formed multicellular aggregates that were not observed in DPSCs or SHEDs. This feature was observed without an apparent difference in the overall osteogenic phenotype.

Analysis of proliferative activity revealed a broadly consistent response to osteogenic induction across all three cell populations (Fig. 2). All CM groups showed continuous growth throughout the cultivation period, reaching maximal cell densities between D5 and D10. In contrast, OM cultures displayed only a modest increase in proliferation during the early stages, followed by a pronounced decline after D5. The decrease coincided with progressive ECM deposition and mineralization, with a plateau phase between D10 and D15. In spite of minor differences in absolute proliferation rates, the three cell types followed comparable growth patterns during osteogenic differentiation.

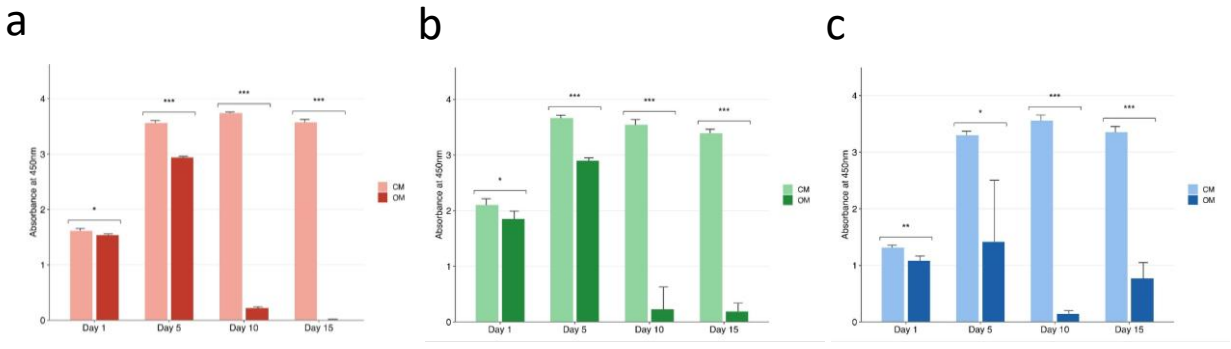


Fig. 2 Cell proliferation during a 15-day culture period under control (CM) and osteogenic (OM) conditions assessed by the CCK-8 assay. Absorbance values, proportional to the number of metabolically active cells, are shown for **a** DPSCs, **b** SHEDs, and **c** NHOst cells. Data are presented as mean ± SD. Statistical comparisons between CM and OM at individual time points were performed separately for each donor-derived cell population; corresponding *p*-values are indicated as $p \leq 0.05$ (*), $p \leq 0.01$ (**), and $p \leq 0.001$ (***).

Matrix mineralization across osteogenic cell populations

To confirm osteogenic differentiation, ECM mineralization was assessed by Alizarin Red S staining and quantified at D5 and D15 (Fig. 3a-b). At D5, calcium deposition remained minimal and did not differ significantly between CM and OM. By D15, OM exhibited intense mineralization at both the macroscopic and microscopic levels, whereas CM remained largely unstained. At this stage, extensive ECM deposition largely masked individual cellular features, consistent with advanced matrix maturation. Quantitative analysis at D15 further confirmed this pattern, revealing approximately 100-fold higher mineralization in OM cultures than in their corresponding CM. Overall, these findings show substantial ECM mineralization under osteogenic conditions in the three donor-derived cell populations examined.

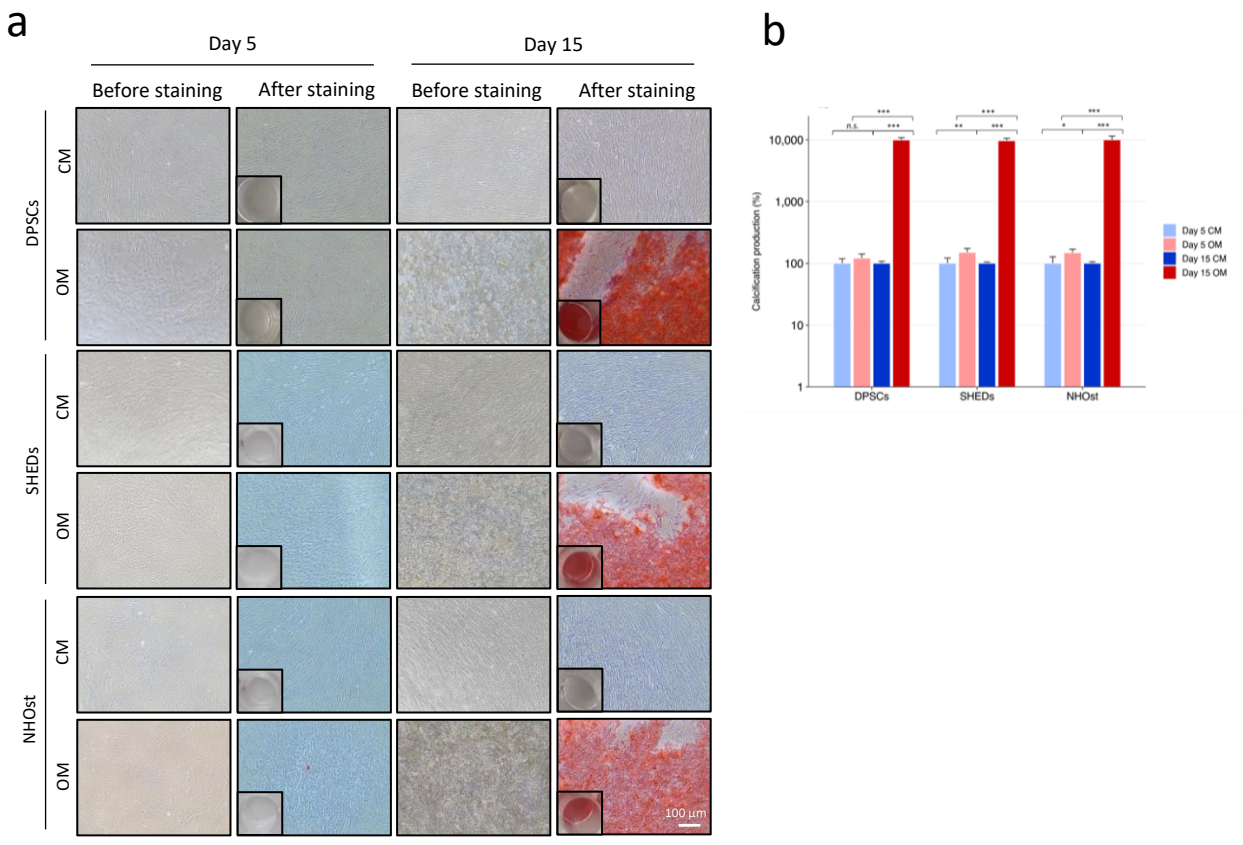
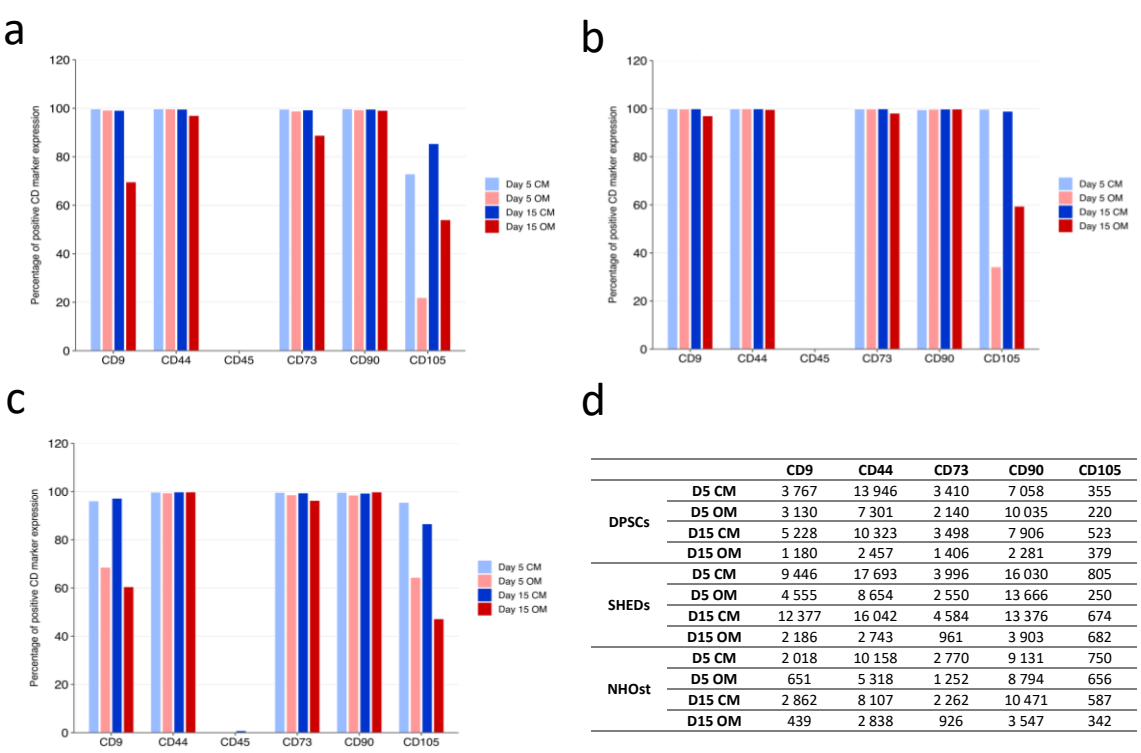


Fig. 3 Alizarin Red S staining of mineral deposits in DPSCs, SHEDs, and NHOst. **a** Macroscopic and microscopic visualization of control (CM) and osteogenically differentiated (OM) samples before and after Alizarin Red S staining on Day 5 (D5) and Day 15 (D15) imaged by light microscopy (100× magnification). **b** Quantification of calcified matrix production. Calcium deposition was normalized to total cellular protein content, with CM values set to 100% at each time point. Data are presented as mean ± SD of three technical replicates. Statistical comparisons between CM and OM were performed separately for each donor-derived cell population at each time point; *p*-values are indicated as $p \leq 0.05$ (*), $p \leq 0.01$ (**), $p \leq 0.001$ (***) and non-significant (*n.s.*).

Maintenance of mesenchymal surface marker expression during osteogenic differentiation

Surface marker expression (CD9, CD44, CD45, CD73, CD90, and CD105) was analyzed by flow cytometry in CM and OM cultures. Across all cell types, the majority of MSC-associated markers remained detectable at high proportions throughout the differentiation period. CD44, CD73, and CD90 were detected in more than 97% of cells in most experimental groups, whereas CD45 expression remained below 1% under all conditions (Fig. 4a-c). Representative histograms showed relatively homogeneous cell populations in DPSCs and SHEDs cultured under CM and OM conditions at D5 (Fig. S2-4). By D15, broader peak distributions and subtle leftward shifts of several positive markers became apparent, suggesting increased population heterogeneity accompanied by reduced fluorescence intensity. Similar changes were observed in NHOst cultures, where shifts in fluorescence intensity profiles were already evident at D5 and persisted throughout osteogenic differentiation. Although the proportion of marker-positive cells remained largely unchanged, the progressive leftward shifts in fluorescence intensity distributions suggested reduced marker expression levels during differentiation. This trend was confirmed by MFI analysis (Fig. 4d). Across all three cell types, MFI progressively declined from D5 to D15, with the most pronounced reductions observed for CD44 and CD90. At D15, MFI decreased by more than 70% in DPSCs and SHEDs and by more than 65% in NHOst cells. An exception was observed for CD90 in DPSCs, where MFI transiently increased by more than 40% at D5 under OM conditions before declining at D15. Notably, a similar transient increase in CD90 MFI was also observed in our previous study [14]. This response was not observed in SHEDs or NHOst cells. Overall, these results indicate that osteogenic differentiation is associated with gradual remodeling of the cell surface phenotype, reflected primarily by reduced MFI of MSC-associated markers rather than a substantial loss of marker-positive cells, while high proportions of marker-positive cells (>97% for CD44, CD73, and CD90 in most experimental groups) were maintained throughout differentiation.



		CD9	CD44	CD73	CD90	CD105
DPSCs	D5 CM	3 767	13 946	3 410	7 058	355
	D5 OM	3 130	7 301	2 140	10 035	220
	D15 CM	5 228	10 323	3 498	7 906	523
	D15 OM	1 180	2 457	1 406	2 281	379
SHEDs	D5 CM	9 446	17 693	3 996	16 030	805
	D5 OM	4 555	8 654	2 550	13 666	250
	D15 CM	12 377	16 042	4 584	13 376	674
	D15 OM	2 186	2 743	961	3 903	682
NHOst	D5 CM	2 018	10 158	2 770	9 131	750
	D5 OM	651	5 318	1 252	8 794	656
	D15 CM	2 862	8 107	2 262	10 471	587
	D15 OM	439	2 838	926	3 547	342

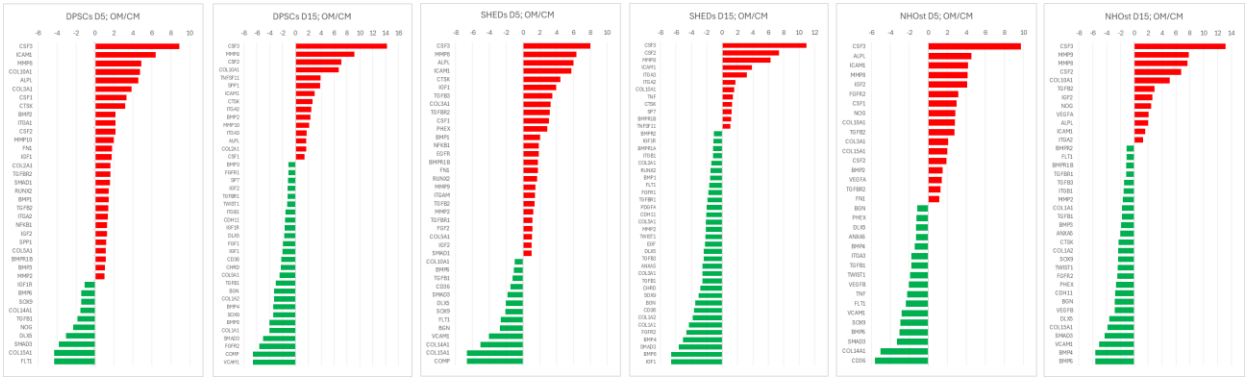
Fig. 4 Distribution of percentage representation of selected surface CD markers positive in analysed cells. Overview of surface CD marker expression in **a** DPSCs, **b** SHEDs, and **c** NHOst cells cultured under control (CM, blue) and osteogenic (OM, red) conditions on Day 5 (D5) and Day 15 (D15). **d** Representative mean fluorescence intensity (MFI) values demonstrate a time-dependent decrease in the expression of selected surface markers with each cell type represented by a single donor-derived cell population, at D5 and D15.

Coordinated transcriptional changes accompany osteogenic differentiation

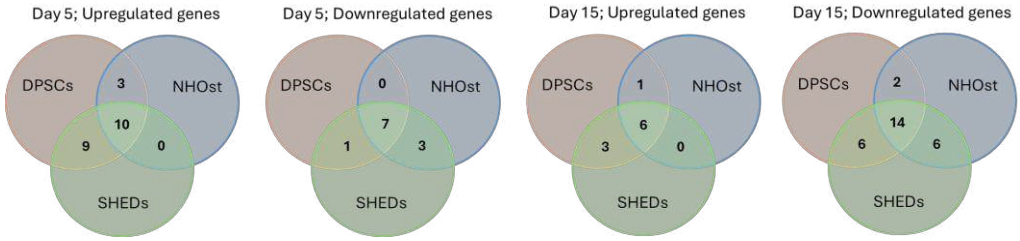
To characterize gene expression changes associated with osteogenic differentiation, the expression of 84 osteogenesis-related genes was analyzed using the RT2 Profiler PCR Array in DPSCs, SHEDs, and NHOst at D5 and D15 (Fig. 5a-c; Table S1). Gene expression levels in OM were compared with time-matched CM using $|\log2FC| \geq 1$. At D5, all three cell populations exhibited increased expression of the canonical osteogenic marker *ALPL*, with log2FC values ranging from 4.51 to 6.00. This transcriptional response also included genes associated with ECM molecules (*COL3A1, FN1, ICAM1*), growth factors and receptors (*IGF2, TGFB2, TGFBR2*), and calcium ion binding and homeostasis (*MMP8*). Notably, *CSF3* (growth factor/cytokine) was the most strongly induced transcript across all cell types (8.00 to 9.73). Strong induction was also observed for *ICAM1* (4.17 to 6.39) and *MMP8* (4.11 to 6.35), indicating a shared early transcriptional response among the three cell types. In contrast, the osteogenic transcription factor *RUNX2* (1.46 to 1.65) was upregulated exclusively in DSCs, together with other

osteogenesis-related genes, including *BMP1, BMPR1B, COL5A1, CTSK, IGF1, MMP2, NFKB1*, and *SMAD1*.

a



b



c

	Day 5 Upregulated genes	Day 5 Downregulated genes	Day 15 Upregulated genes	Day 15 Downregulated genes
DPSCs SHEDs NHOst	*ALPL, COL3A1, CSF1, CSF3, FN1, ICAM1, IGF2, MMP8, TGFB2, TGFBR2*	*BMP6, COL14A1, DLX5, FLT1, SMAD3, SOX9, TGFB1*	*COL10A1, CSF2, CSF3, ICAM1, ITGA2, MMP8*	*BGN, BMP4, BMP6, CDH11, COL1A1, COL1A2, DLX5, FGFR2, ITGB1, SMAD3, SOX9, TGFB1, TGFBR1, TWIST1*
DPSCs SHEDs	*BMP1, BMPR1B, COL5A1, CTSK, IGF1, MMP2, NFKB1, RUNX2, SMAD1*	*COL15A1*	*CTSK, ITGA3, TNFSF11*	*CD36, COL5A1, FGFR1, CHRD, IGF1, IGF1R*
DPSCs NHOst	*BMP2, COL10A1, CSF2*	none	*ALPL*	*BMP3, VCAM1*
SHEDs NHOst	none	*BGN, CD36, VCAM*	none	*ANXA5, BMPR2, FLT1, ITGB1, MMP2, TGFB3*

Fig. 5 Comparative gene expression profiles obtained by RT2 Profiler PCR Array analysis following osteogenic induction. **a** Gene expression changes in osteogenically differentiated cells (OM) relative to their corresponding control cultures (CM) in DPSCs, SHEDs, and NHOst cells with each cell type represented by a single donor-derived cell population, at D5 and D15. Genes with $|\log2FC| \geq 1$ were classified as upregulated (red) and downregulated (green). **b** Venn diagrams illustrating shared and cell type-specific sets of upregulated and downregulated genes among DPSCs, SHEDs, and NHOst cells at Day 5 (D5) and Day 15 (D15) of osteogenic differentiation. **c** List of upregulated and downregulated genes identified in DPSCs, SHEDs, and NHOst cells following osteogenic induction at D5 and D15.

DPSCs exhibited altered expression of 38 genes (28 upregulated, 10 downregulated), SHEDs exhibited 39 genes (26 upregulated, 13 downregulated), and NHOst cells exhibited 34 genes (17 upregulated, 17 downregulated). In all three populations, upregulated genes outnumbered downregulated genes at D5, reflecting extensive changes in transcriptional profiles during the early

phase of osteogenic differentiation. By D15, the number of genes meeting the predefined expression-change threshold further increased to 41 in DPSCs (15 upregulated, 26 downregulated), 44 in SHEDs (12 upregulated, 32 downregulated), and 38 in NHOst cells (12 upregulated, 26 downregulated). However, the transcriptional landscape shifted toward predominance of gene repression. Several genes associated with developmental and growth factor signaling, including *BMP6, DLX5, SOX9, SMAD3*, and *TGFB1,* were consistently downregulated across cell populations and time. Despite the predominance of downregulated transcripts, a subset of genes remained strongly induced in all three cell types, including *CSF3* (10.91 to 14.23), *MMP8* (6.26 to 9.15), *CSF2* (6.76 to 7.38), and *COL10A1* (1.57 to 6.72). Additional induction was observed for genes associated with cell adhesion and matrix interactions, including *ICAM1* and *ITGA2*. Collectively, these transcriptional changes are consistent with coordinated remodeling of gene expression programs associated with osteogenic differentiation, including cytokine-associated signaling, developmental regulation, ECM remodeling, and cell-matrix interactions.

Validation of osteogenic and matrix-remodeling gene expression patterns

To independently validate the gene expression patterns identified by the RT2 Profiler PCR Array, selected osteogenesis-related genes were analyzed by RT-qPCR using a custom-designed validation panel (Fig. 6a-b). Overall, the validation analysis reproduced the major expression trends observed in the array dataset, supporting the consistency of the observed transcriptional patterns across the two analytical approaches (Fig. S5). Genes exhibiting sustained upregulation in the PCR array analysis, including *ALPL, COL10A1, CSF3, ICAM1,* and *MMP8*, exhibited comparable expression patterns in the validation experiments across all three cell populations. *ALPL* (4.41 to 5.43) and *ICAM1* (4.60 to 6.31) showed their strongest induction at D5, followed by a moderate decline at D15 (*ALPL*: 1.68 to 2.26; *ICAM1*: 1.64 to 3.68). Additionally, sustained induction of several genes was observed throughout osteogenic differentiation. Among these, *MMP8* was progressively upregulated from D5 (4.99 to 5.82) to D15 (6.20 to 8.60), whereas *COL10A1* exhibited a more pronounced induction by D15 (1.60 to 5.85)

compared with D5 (-1.02 to 4.47). *CSF3* represented the most strongly induced transcript in all cell types, increasing from D5 (9.32 to 10.51) to D15 (12.14 to 15.59).

a

Full name of gene	Symbol	Day	DPSCs log2FC	SHEDs log2FC	NHOst log2FC
Alkaline phosphatase, liver/bone/kidney	*ALPL*	5	4.410	5.427	4.862
		15	1.749	1.680	2.259
Bone morphogenetic protein 4	*BMP4*	5	0.337	-1.146	-1.161
		15	-2.917	-5.687	-5.791
Collagen, type X, alpha	*COL10A1*	5	4.469	-1.024	3.419
		15	5.845	1.602	5.802
Collagen, type XIV, alpha 1	*COL14A1*	5	-1.473	-5.793	-4.911
		15	-9.152	-11.682	-10.739
Cartilage oligomeric matrix protein	*COMP*	5	-1.032	-7.541	-7.961
		15	-7.977	-12.573	-15.602
Colony stimulating factor 3 (granulocyte)	*CSF3*	5	9.324	10.043	10.507
		15	15.592	12.139	14.984
Intercellular adhesion molecule 1	*ICAM1*	5	6.314	5.436	4.595
		15	2.853	3.677	1.644
Insulin-like growth factor 1 (somatomedin C)	*IGF1*	5	1.574	3.201	1.183
		15	-1.801	-7.668	-11.184
Matrix metallopeptidase 8	*MMP8*	5	5.819	5.686	4.987
		15	8.602	6.195	7.988
Vascular cell adhesion molecule 1	*VCAM1*	5	0.545	-4.529	-2.556
		15	-7.125	-10.000	-5.400

b

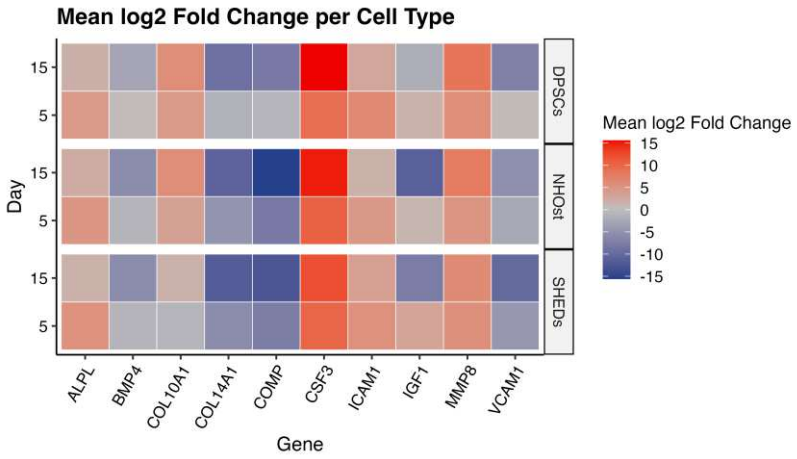


Fig. 6 Gene expression of selected genes during osteogenic differentiation. The expression of *ALPL, BMP4, COL10A1, COL14A1, COMP, CSF3, ICAM1, IGF1, MMP8*, and *VCAM1* was quantified by RT-qPCR in DPSCs, SHEDs, and NHOst at Day 5 (D5) and Day 15 (D15) of osteogenic differentiation. **a** The table presents log2FC values calculated as the expression ratio between osteogenic (OM) and control (CM) conditions at each time point. **b** The heatmap summarizes mean log2FC values illustrating overall patterns of transcriptional regulation across the three donor-derived cell populations, with each cell type represented by a single donor-derived population.

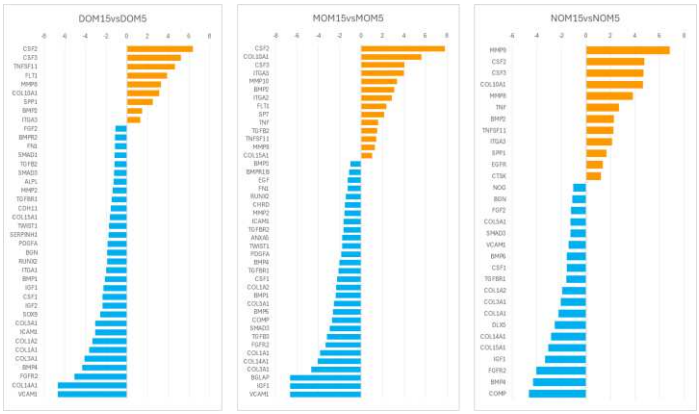
The validation analysis likewise recapitulated the downregulation of *BMP4, COL14A1, COMP*, and *VCAM1* observed in the PCR array dataset with the strongest suppression observed at late osteogenesis. Particularly decreased expression was observed in *COL14A1* (-9.15 to -11.68), *COMP* (-7.98 to -15.60), and *VCAM1* (-5.40 to -10.00) at D15. *IGF1* displayed a unique temporal expression

profile with transient upregulation at D5 (1.18 to 3.20) followed by downregulation at D15 (-1.80 to -11.18). Heatmap analysis (Fig. 6b) showed similar temporal expression patterns across the three cell populations, consistent with the transcriptional changes observed during osteogenic differentiation.

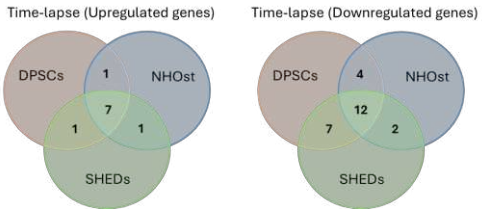
Molecular progression during osteogenic differentiation and matrix maturation

Temporal changes in gene expression during osteogenic differentiation were assessed by comparing D15 and D5 transcriptomic profiles of OM cultures (Fig. 7a-c). Overall, the transcriptomic landscape shifted toward gene repression in all three cell populations. Accordingly, 40 genes met the predefined expression-change threshold in DPSCs (9 upregulated and 31 downregulated), 43 in SHEDs (14 upregulated and 29 downregulated), and 31 in NHOst cells (12 upregulated and 19 downregulated) (Table S2).

a



b



c

	OM D15/D5 Upregulated genes	OM D15/D5 Downregulated genes
DPSCs, SHEDs, NHOst	*BMP2, COL10A1, CSF2, CSF3, ITGA3, MMP8, TNFSF11*	*BMP4, COL14A1, COL1A1, COL1A2, COL3A1, COL5A1, CSF1, FGFR2, IGF1, SMAD3, TGFBR1, VCAM1*
DPSCs, SHEDs	*FLT1*	*BMP1, COL5A1, ICAM1, MMP2, PDGFA, RUNX2, TWIST1*
DPSCs, NHOst	*SPP1*	*BGN, COL15A1, FGF2, FN1*
SHEDs, NHOst	*TNF*	*BMP6, COMP*

Fig. 7 Time-specific patterns of gene expression changes during osteogenic differentiation. **a** Gene expression changes in osteogenically differentiated DPSCs, SHEDs, and NHOst cells at Day 15 (D15) relative to Day 5 (D5). Genes with |log2FC| ≥ 1 were classified as upregulated (orange) and downregulated (blue), respectively. **b** Venn diagrams illustrating cell type-specific and overlapping sets of upregulated and downregulated genes identified at D15/D5 in DPSCs, SHEDs, and NHOst cells. **c** List of genes showing temporal upregulation or downregulation in each donor-derived cell population (D15 vs. D5), with each cell type represented by a single donor-derived population.

Seven genes remained upregulated across all three cell populations, including genes associated with skeletal development (*BMP2, COL10A1*), growth factors and receptors (*CSF2, CSF3*), calcium ion binding and homeostasis (*MMP8*), and cell adhesion (*ITGA3, TNFSF11*). Among these, *CSF3* and *MMP8* exhibited the strongest and most sustained induction across the differentiation period. In contrast, during later stages of osteogenic differentiation, coordinated downregulation was observed among genes associated with ECM molecules (*COL1A1, COL1A2, COL3A1, COL5A1, COL14A1*), growth factors and receptors (*BMP4, CSF1, FGFR2, IGF1, TGFBR1*), and cell growth and proliferation (*SMAD3, VCAM1*). This may reflect continued transcriptional refinement during osteogenic maturation.

Protein redistribution during ECM assembly

Immunocytochemical analysis revealed extensive fluorescence signals and subcellular localization patterns for osteogenesis-associated markers with pronounced cytoskeletal reorganization in DPSCs (Fig. 8a; Fig. S6), SHEDs (Fig. 8b; Fig. S7), and NHOst cells (Fig. 8c; Fig. S8), including APOA2, BSP2, COL1A1, DMP1, DSPP, OPN, and F-actin. Fluorescence of phalloidin (F-actin) decreased about 62−69% compared to CM at D15, which may indicate substantial restructuring of the cytoskeleton during osteogenic maturation. Concurrently, fluorescence signals for multiple matrix-associated proteins increased and showed marked redistribution from predominantly cytoplasmic localization toward perinuclear and ECM-associated patterns. Despite these common features, individual osteogenic markers exhibited distinct temporal dynamics among the three donor-derived cultures. DPSCs showed sustained increases in APOA2, DMP1, and BSP2 fluorescence signals, with BSP2 showing the strongest response (approximately 420% of CM levels at D15), whereas COL1A1, DSPP, and OPN peaked early at D5. SHEDs displayed a prolonged increase in ECM-associated fluorescence signals, characterized by marked induction of COL1A1 (365% of CM levels at D15) together with progressive increases in APOA2 and DSPP, while BSP2, DMP1, and OPN reached maximal fluorescence intnsity at D5 before partially declining. In contrast, NHOst cells mounted a rapid early matrix response, with maximal induction of COL1A1 (618% of CM levels), APOA2, BSP2, OPN, and DMP1 already at D5, followed by declining

fluorescence at D15, consistent with an earlier transition toward later stages of matrix maturation. DSPP fluorescence remained elevated throughout late differentiation. Across the three donor-derived cultures, the observed marker remodeling followed a broadly similar temporal pattern, with differences primarily in the timing and magnitude of individual marker-associated fluorescence.

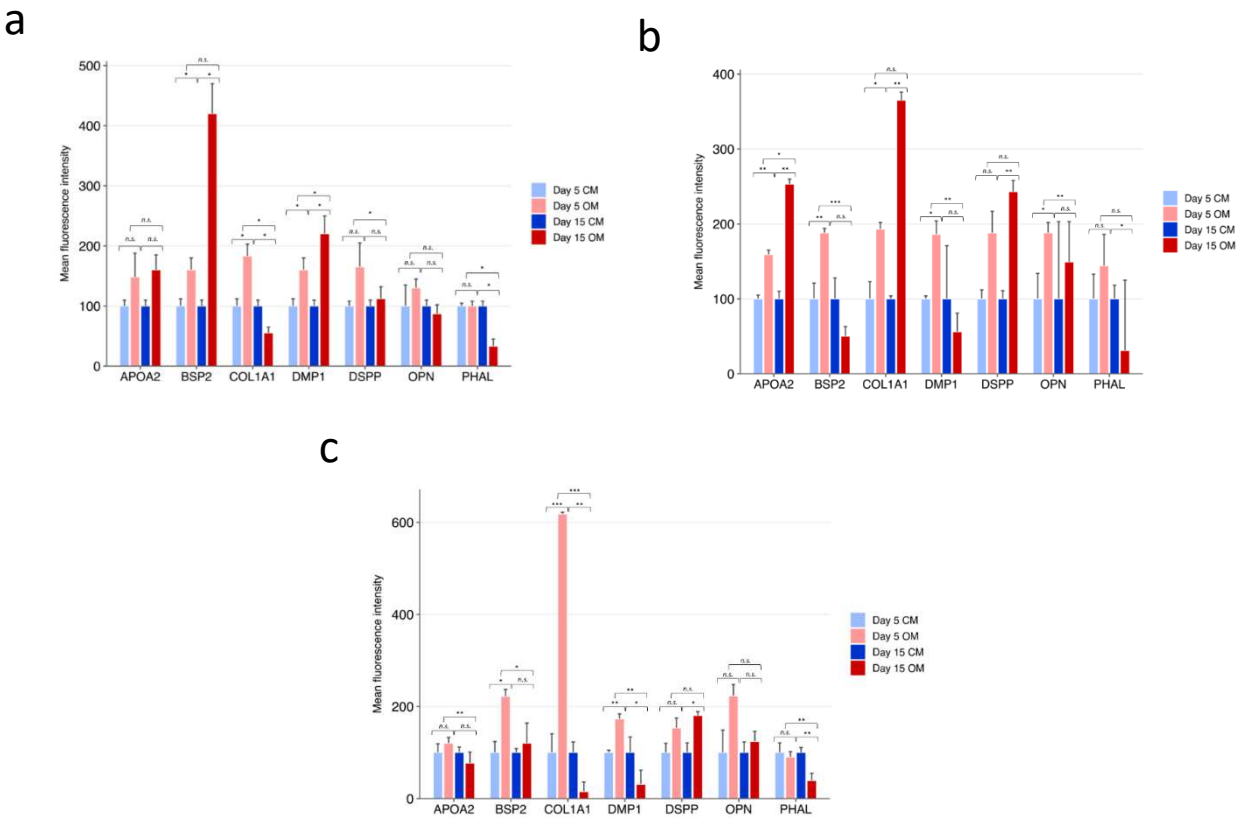


Fig. 8 Immunocytochemical quantification of osteogenesis-related protein expression**.** Mean fluorescence intensity (MFI) was quantified for individual proteins in **a** DPSCs, **b** SHEDs, and **c** NHOst at Day 5 (D5) and Day 15 (D15) of osteogenic differentiation. Expression levels were normalized to corresponding controls (CM), which were set to 100% at each time point. Statistical comparisons between osteogenic (OM) and control (CM) conditions were performed separately for each donor-derived cell population at each time point; *p*-values are indicated as $p \leq 0.05$ (*), $p \leq 0.01$ (**), and $p \leq 0.001$ (***); *n.s.,* not significant.

Intracellular metabolomic remodeling

Targeted metabolomic profiling of cell lysates identified intracellular metabolic changes associated with osteogenic induction in DPSCs, SHEDs, and NHOst cultures (Fig. 9a, b; Table S3). Although several differences between the three donor-derived cultures were observed, multiple metabolic signatures were shared across all three cell populations. Three amino acids showed increased intracellular levels

at both D5 and D15, namely phenylalanine (1.09 to 2.60), isoleucine (1.40 to 2.43), and threonine (1.59 to 5.42). Threonine accumulation was most pronounced in the NHOst culture, where tryptophan also exhibited a similar trend (2.95 to 3.34). Additional amino acids that increased during differentiation included proline, serine, and valine. One of the most consistent changes was observed for *trans*-4-hydroxyproline, which showed a similar increase across the three donor-derived cultures at D5 (1.99 to 2.75). In contrast, alanine decreased specifically in DSCs compared with NHOst. Moreover, ornithine, tyrosine and α-aminoadipic acid showed markedly reduced intracellular levels following osteogenic induction predominantly in DSCs. Changes in glutamine metabolism were reflected by a decreased glutamine-to-glutamate ratio in NHOst at both time points and in DSCs at D15.

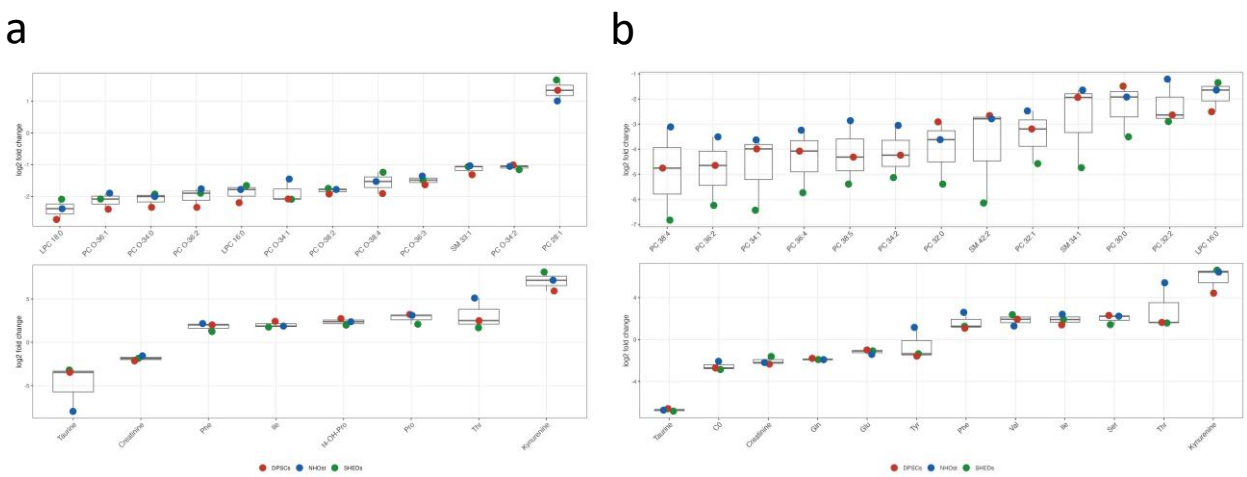


Fig. 9 Boxplots of intracellular metabolite changes. Analyses were performed on cell lysates obtained from DPSCs, SHEDs, and NHOst at **a** Day 5 (D5) and **b** Day 15 (D15) with each cell type represented by a single donor-derived cell population. Metabolite changes are expressed as log2FC between osteogenic and control conditions (OM/CM). Metabolites detected in all three cell types and meeting the FC criterion (|log2FC| ≥ 1) are displayed as boxplots. Negative log2FC values indicate lower metabolite abundance in OM relative to CM, whereas positive values indicate higher abundance in OM relative to CM. Metabolites are designated using standard nomenclature. Standard abbreviations are used for amino acids and biogenic amines; C0, carnitines; LPC, lysophosphatidylcholines; PC, phosphatidylcholines; PC O, ether-linked phosphatidylcholines; SM, sphingomyelins.

Among the biogenic amines, kynurenine showed the largest increase following osteogenic induction, with an approximately 20-fold to >1000-fold increase in OM across the three donor-derived cultures. Putrescine increased in OM DSCs at D15, whereas taurine exhibited one of the strongest decreases detected following osteogenic induction especially at D15 (-6.59 to -6.83). Additional metabolites were likewise altered during differentiation. Intracellular creatinine remained decreased

in OM at both time points, whereas intracellular hexoses were reduced, particularly in DSCs at D15. The majority of intracellular phosphatidylcholines, ether-linked phosphatidylcholines, and sphingomyelins showed reduced abundance in all three OM, consistent with coordinated lipid remodeling during osteogenic induction. In contrast, only a limited number of phosphatidylcholines increased, predominantly at D5. Among these, PC 28:1 was elevated at both time points.

Dynamics of the intracellular metabolome

Longitudinal analysis (D15/D5) revealed marked metabolic remodeling during osteogenic differentiation (Table S4). Across all three cell populations, most metabolites showing substantial changes exhibited lower intracellular abundance at D15 than at D5, indicating a predominantly decreasing metabolic pattern over this interval. Common temporal changes included decreased intracellular levels of aspartate, serine, and hexoses (-1.13 to -1.59), whereas creatinine remained relatively stable between D5 and D15. In contrast to these shared temporal trends, DSCs underwent more extensive metabolic remodeling than NHOst cells in the tested cultures, especially in amino acids and biogenic amines. This was characterized by a reduction in the glutamine-to-glutamate ratio together with decreased intracellular levels of asparagine, glycine, N-acetylornithine, kynurenine, methionine sulfoxide, spermidine, spermine, and *trans*-4-hydroxyproline. Kynurenine (-1.01 to -1.88) and taurine (-1.86 to -3.68) exhibited one of the most pronounced temporal declines in DSCs. By comparison, NHOst cells showed a slight increase in intracellular taurine abundance (1.46). At the lipid level, intracellular phospholipid remodeling persisted from D5 to D15. Most lipid subclasses exhibited a further reduction between D5 and D15, while the temporal pattern of lipid remodeling in NHOst closely resembled that observed in DPSCs.

Extracellular metabolomic changes

Compared with the intracellular metabolome, fewer extracellular metabolites fulfilled the selection criteria. Nevertheless, several metabolites showed similar extracellular patterns across all three cell

555 populations, consistent with coordinated changes in the osteogenic secretome (Fig. 10a,b; Tables S5
556 and S6). The extracellular amino acid profile was characterized by increased serine levels across all
557 three cell populations at both D5 (1.99 to 2.43) and D15 (1.35 to 1.61), whereas alanine levels were
558 reduced at both time points. N-acetylornithine also increased at D5 (1.18 to 2.32). Tryptophan
559 exhibited the strongest extracellular accumulation at D15 across all cell populations (2.17 to 4.74),
560 while at D5 an increase was detected only in NHOst (5.08). Kynurenine emerged as the most prominent
561 extracellular metabolic feature associated with osteogenic differentiation. Conditioned media from
562 OM contained markedly higher kynurenine levels than CM at both D5 (6.66 to 10.76) and D15 (6.83 to
563 9.00), demonstrating consistently elevated extracellular kynurenine levels under osteogenic
564 conditions.

565 Longitudinal analysis of conditioned media revealed relatively fewer changes than were observed
566 intracellularly. Extracellular methionine sulfoxide and asparagine increased between D5 and D15
567 across the cell populations grown in OM whereas isoleucine decreased over time in DSCs (-1.71 to -
568 4.79). In contrast, extracellular kynurenine levels remained relatively stable between D5 and D15.

569

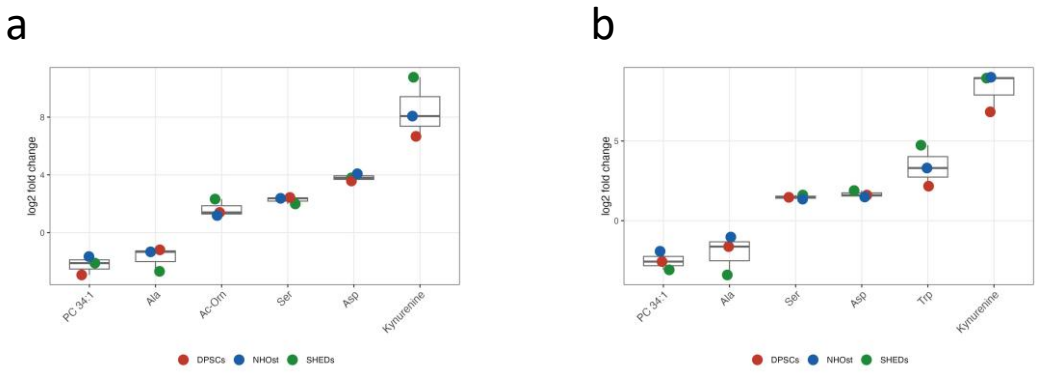


Fig. 10 Boxplots of extracellular metabolite changes. Analyses were performed on conditioned media obtained from DPSCs, SHEDs, and NHOst at **a** Day 5 (D5) and **b** Day 15 (D15) with each cell type represented by a single donor-derived cell population. Metabolite changes are expressed as log2FC between osteogenic and control conditions (OM/CM). Metabolites detected in all three cell types and meeting the predefined FC criterion ($|log2FC| \geq 1$) are displayed as box plots. Negative log2FC values indicate lower metabolite abundance under OM relative to CM, whereas positive values indicate higher abundance in OM relative to CM. Metabolites are designated using standard nomenclature. Standard abbreviations are used for amino acids and biogenic amines; PC, phosphatidylcholines.

570

571

Discussion

Continuous bone remodeling is essential for maintaining skeletal integrity and mineral homeostasis. Although small bone defects generally heal spontaneously, regeneration of large segmental defects resulting from trauma, tumor resection, or age-related disorders often requires additional therapeutic intervention [24]. MSCs have therefore emerged as promising candidates for bone regeneration owing to their capacity to modulate tissue repair through paracrine signaling, immunomodulatory activity, and differentiation toward the osteoblastic lineage [25]. Within this context, a central aim of the present study was to assess the extent to which DSCs recapitulate key features of the osteogenic program observed in primary NHOst. Through integrated functional, phenotypic, transcriptomic, protein, and metabolomic analyses, we found that the examined donor-derived DPSCs, SHEDs, and primary NHOst preparations shared multiple characteristics of osteogenic differentiation. This overall convergence across the three cellular preparations is noteworthy. However, because each cell population was represented by a single donor, the present design cannot distinguish cell-type effects from donor-specific effects or establish inter-donor generalizability. Accordingly, differences observed among DPSCs, SHEDs, and NHOst should be interpreted within the context of the donor-derived preparations examined, while their broader cell-type specificity remains to be established across independent donors. Nevertheless, the concordance observed across multiple analytical levels provides new insight into the biological relationship between DSCs and NHOst within the present experimental system and may supports the potential utility of DSCs as a model for bone regeneration research.

Morphological changes represented one of the earliest visible evidence of osteogenic differentiation, with all three cell populations undergoing a comparable transition toward a bone-forming phenotype accompanied by ECM mineralization, whereas CM retained a stable spindle-shaped, elongated morphology [15,26]. In line with their immature phenotype, CM continued to proliferate throughout cultivation, with SHEDs exhibiting the highest proliferative activity, in agreement with previous reports describing their shorter population doubling time and greater

proliferative capacity than DPSCs [6,27]. In contrast, the decline in proliferation observed after osteogenic induction, followed by a plateau after D10 was consistent with the transition from cell expansion to matrix maturation and mineralization. A similar pattern was previously described during osteogenic differentiation by Carluccio *et al.* [28]. Progressive calcium deposition in all three cell populations further supports comparable osteogenic maturation of DPSCs, SHEDs, and NHOst, corroborating earlier reports demonstrating similar mineralization dynamics [14,29].

A notable observation was the overall stability of the mesenchymal immunophenotype throughout osteogenic differentiation. In spite of extensive transcriptional remodeling and progressive cellular maturation, DPSCs, SHEDs, and NHOst remained predominantly positive for the commonly used mesenchymal surface markers CD44, CD73, and CD90, whereas the proportion of CD105-positive cells declined only modestly, particularly after osteogenic induction. CD45 expression was absent in all cell populations throughout the study. These data suggest that osteogenic differentiation involved phenotypic adaptation while largely preserving the characteristic mesenchymal surface marker profile, as previously observed in MSCs [30,31]. A distinct pattern emerged when marker-associated fluorescence intensity was evaluated. MFI decreased markedly for CD44, CD73, CD90, and especially CD105 following osteogenic differentiation, indicating a substantial shift in surface marker-associated fluorescence during acquisition of osteoblast-like characteristics. Moreover, CD9 displayed a different behavior from the remaining markers. While SHEDs largely preserved the proportion of CD9-positive cells after differentiation, MFI declined across all three cell populations. These findings further support the concept that differentiation is associated not only with lineage-specific gene expression but also with changes in the surface immunophenotype. Although marker positivity was largely maintained throughout differentiation, the MFI of individual surface markers continued to change, indicating that marker positivity alone does not necessarily reflect stable surface expression. Similar reductions in MSCs marker density have also been reported previously [32-34].

One of the most striking findings of this study was the broad similarity in osteogenic transcriptional responses across DPSCs, SHEDs, and NHOst cells. Early differentiation was characterized by induction

of canonical osteogenic regulators, including *ALPL* and *RUNX2*, alongside activation of genes involved in ECM organization and microenvironmental remodeling. This transcriptional signature reflects the coordinated interplay between matrix synthesis, degradation, and cell-matrix interactions required for successful osteogenic differentiation, reinforcing earlier evidence in this field [35,36]. As differentiation progressed, a distinct transcriptional shift became apparent, moving from matrix production toward matrix maturation and mineralization. Persistent expression of *ALPL* and *COL10A1* supports ongoing osteogenic maturation, while the concurrent decrease in *COL1A1, COL1A2,* and *IGF1* expression may reflect stage-specific remodeling of the osteogenic transcriptional program associated with late-stage mineralization. This interpretation aligns with evidence that osteoblast differentiation involves dynamic changes in extracellular matrix production and inflammatory signaling, which can both promote and fine-tune osteogenesis in a context- and intensity-dependent manner [37]. Notably, sustained *MMP8* upregulation suggests that ECM remodeling remains an active component of osteogenic maturation rather than being restricted to early differentiation stages. Although *MMP8* is not considered a classical osteogenic marker, its induction across all three cell populations points to a broader role for ECM remodeling in shaping the extracellular environment associated with mineral deposition. Particularly noteworthy was the robust and sustained induction of *CSF3*, which emerged as one of the most prominently upregulated transcripts throughout osteogenic differentiation. While traditionally associated with hematopoietic regulation, accumulating evidence indicates that CSF3 also contributes to osteogenesis, supporting the view that cytokine signaling may represent an integral component of the osteogenic differentiation process. Consistent with this concept, MSCs actively secrete cytokines that regulate the bone microenvironment and coordinate regenerative processes [38-41]. Together with the shared regulation of *COL10A1, ICAM1,* and *MMP8*, these findings suggest that the osteogenic programs observed across the examined cell populations extend beyond canonical markers such as *RUNX2* and *ALPL*, encompassing coordinated regulation of ECM remodeling, cytokine-mediated signaling, and microenvironmental adaptation.

Immunocytochemical analyses provided complementary evidence of coordinated remodeling involving cellular metabolism, ECM organization, and cytoskeletal architecture in each cell-specific population. A prominent finding was the progressive extracellular accumulation of APOA2-associated fluorescence, supporting the emerging role of lipid metabolism in osteogenic maturation [17,42,43]. In parallel, lipid remodeling was observed in our metabolomic analysis. Dynamic ECM reorganization was reflected by persistent extracellular COL1A1-associated signal, while *COL1A1* transcript levels and intracellular fluorescence declined and *MMP8* expression remained persistent, supporting ongoing matrix organization. This interpretation is supported by previous studies demonstrating continuous collagen reorganization during the formation of mineralized bone tissue and osteocyte-associated lacunar structures [11]. Likewise, BSP2, DSPP, DMP1, and OPN supported progression toward a mature osteogenic phenotype despite differences in their temporal expression patterns. Reduced F-actin staining at D15 further indicated cytoskeletal remodeling associated with matrix formation and mineralization [44,45]. Although temporal protein dynamics varied more than transcriptional responses, all three cell populations converged toward a comparable osteogenic phenotype, suggesting that similar phenotypic outcomes can arise despite differences in the timing and extent of post-transcriptional and extracellular remodeling. The dynamic nature of ECM organization and its variation among cell types during osteogenic differentiation has been well documented [10,11] and is in line with our findings.

Targeted metabolomic profiling revealed coordinated remodeling of both the intracellular metabolome and the extracellular metabolic milieu during osteogenic differentiation. Previous metabolomic studies of MSC osteogenesis have similarly demonstrated coordinated alterations in amino acid, phospholipid, and sphingolipid metabolism, supporting the concept that metabolic adaptation is an integral component of osteogenic maturation [17,46,47]. Although several differences among the examined cell populations were detected, the overall metabolic response to osteogenic induction was largely shared between DSCs and NHOst. However, longitudinal analysis demonstrated that DSCs underwent substantially more dynamic metabolic remodeling than NHOst, particularly

within amino acid and biogenic amine metabolism. This finding likely reflects the greater metabolic plasticity associated with lineage commitment and differentiation of DSCs, whereas NHOst may undergo more limited metabolic adaptation to support matrix production and mineralization. Amino acid metabolism represented the principal metabolic axis affected by osteogenic differentiation. The osteogenic induction-associated increase in intracellular and extracellular serine, decreased glutamine-to-glutamate ratio, and coordinated alterations in several essential amino acids are in line with the current understanding that osteoblast differentiation involves extensive metabolic reprogramming to sustain biosynthesis, ECM production, and cellular maturation. Notably, intracellular *trans*-4-hydroxyproline levels increased early during osteogenic differentiation in all three cell populations. As *trans*-4-hydroxyproline is closely associated with collagen maturation [48], its early increase is consistent with enhanced collagen maturation and ECM remodeling during osteogenic differentiation. The most distinctive metabolic alteration observed in the present study was the marked intracellular accumulation and extracellular release of kynurenine. To our knowledge, this is the first study to characterize intracellular kynurenine accumulation together with its extracellular release during osteogenic differentiation across NHOst, DPSCs, and SHEDs. The observed kynurenine accumulation links osteogenic differentiation with tryptophan metabolism via the kynurenine pathway, the major route of tryptophan degradation in mammalian cells [49]. Increasing evidence indicates that tryptophan metabolism contributes to skeletal homeostasis by regulating osteoblast differentiation, osteoclast activity, and immune signaling [50]. Although prolonged exposure to exogenous kynurenine has been associated with oxidative stress, impaired osteoblast bioenergetics, and age-related bone loss [51,52], its physiological role during osteogenic differentiation remains unclear and is likely influenced by cellular context, metabolite concentration, and differentiation stage [53]. Likewise, intracellular phosphatidylcholine and sphingomyelin species were broadly reduced following osteogenic induction, with lipid remodeling continuing throughout differentiation. Given their structural and signaling functions, these changes may reflect altered membrane turnover and vesicular trafficking associated with extracellular remodeling during osteoblast maturation [54].

Overall, the present results show that DSCs acquire key features of primary NHOst during *in vitro* osteogenic differentiation while retaining selected characteristics related to their cellular origin. The principal biological insights emerging from the integrated phenotypic, transcriptomic, protein, and metabolomic analyses are summarized in Table 1. Determining how these common differentiation programs and metabolic adaptations influence bone regeneration *in vivo* will be essential for translating these findings into regenerative applications.

Table 1. Integrated biological interpretation of osteogenic differentiation in DPSCs, SHEDs, and NHOst cells.

Biological level	Shared observations in DPSCs, SHEDs and NHOst	Cell type-specific observations	Biological implication
Morphology	Comparable morphological transition and mineralization	SHEDs showed faster growth rate	Shared osteogenic progression
Immunophenotype	MSC phenotype was largely maintained	CD9 expression remained stable in SHEDs	Osteogenesis with limited changes in MSC phenotype
Transcriptome	Shared osteogenesis-related gene expression patterns	Temporal differences in gene regulation	Shared regulatory network
Protein localization	ECM remodeling and osteogenesis-related protein deposition	Differences in matrix organization	Alternative structural adaptations
Intracellular metabolome	Similar amino acid and lipid remodeling	Early metabolic differences	Metabolic adaptation with cell type-specific features
Extracellular metabolome	Similar patterns of metabolite release	Differences in metabolite abundance	Dynamic metabolic communication
Novel findings	Increased transcription of *CSF3*, *ICAM1*, and *MMP8*, together with endogenous kynurenine production and release	Persistent cell type-specific differences despite shared osteogenic characteristics	Previously underrecognized aspect of the osteogenic differentiation *in vitro*

Several limitations of the present study should be acknowledged. First, the comparative analyses were performed using single donor-derived DPSCs, SHEDs, and NHOst populations, precluding assessment of donor-to-donor variability. Second, transcriptional profiling was restricted to a targeted osteogenesis-focused gene panel and two differentiation time points, which may not fully capture the complexity and temporal dynamics of osteogenic progression. Finally, the transcriptomic and metabolomic findings require validation across larger donor cohorts to establish their generalizability. Future studies integrating high-resolution transcriptomic, single-cell, and functional *in vivo* approaches will be important to further define the regulatory mechanisms underlying osteogenic differentiation

and to determine the translational relevance of the osteogenic programs identified across the examined cell populations.

Conclusion

Using integrated comprehensive analyses, we show that DSCs acquire the defining characteristics of primary NHOst during physiologically relevant *in vitro* osteogenic differentiation while preserving selected features related to their cellular origin. Rather than indicating fundamentally distinct osteogenic trajectories, the observed molecular and metabolic differences occurred alongside convergence toward a common osteoblast-like phenotype. Beyond canonical osteogenic markers, we identified a shared transcriptional signature involving sustained induction of *CSF3, ICAM1,* and *MMP8* suggesting coordinated regulation of ECM remodeling and microenvironmental adaptation during osteogenesis. In addition, the coordinated intracellular accumulation and extracellular release of kynurenine identifies a previously underrecognized metabolic feature of *in vitro* osteogenic differentiation. These findings provide an integrated framework linking phenotypic, transcriptional, protein, and metabolic remodeling and further support the translational potential of DSCs for BTE and RM.

List of abbreviations

ALPL/ALP	Alkaline phosphatase gene/protein
APO	Apolipoprotein
BMP	Bone morphogenetic protein
BSA	Bovine serum albumin
BSP	Bone sialoprotein
BTE	Bone tissue engineering
CCK-8	Cell counting kit 8
CM	Cells grown in control medium

744	COL-	Collagen-type
745	COMP	Cartilage oligomeric matrix protein
746	CSF	Colony stimulating factor
747	CTSK	Cathepsin K
748	DLX5	Distal-less homeobox 5
749	DMP1	Dentin matrix protein 1
750	DPBS	Dulbecco´s phosphate buffered saline
751	DPSCs	Mesenchymal stromal cells isolated from adult dental pulp
752	DSCs	Dental tissue-derived mesenchymal stromal cells
753	DSPP	Dentin sialophosphoprotein
754	ECM	Extracellular matrix
755	FBS	Fetal bovine serum
756	FGF	Fibroblast growth factor
757	FC	Fold change
758	FLT1	Fms-related tyrosine kinase 1
759	FN1	Fibronectin 1
760	CHRD	Chordin
761	ICAM1	Intracellular adhesion molecule 1
762	IGF1	Insulin-like growth factor 1
763	ITGA 3	Integrin alpha 3
764	MSCs	Mesenchymal stromal cells
765	MMP	Matrix metalopeptidase
766	NHOst	Normal human osteoblasts
767	OCN	Osteocalcin
768	OM	Cells grown in osteogenic differentiation medium
769	OPN	Osteopontin

OSX	Osterix
PDGFA	Platelet derived growth factor subunit A
PHEX	Phosphatase-regulating endopeptidase homolog X-linked
RM	Regenerative medicine
RT	Room temperature
RUNX2	Runt-related transcription factor 2
SHEDs	Mesenchymal stromal cells isolated from exfoliated deciduous teeth
SMAD3	Mothers against decapentaplegic homolog 3
SOX9	SRY-box transcription factor 9
TGF	Transforming growth factor
TNF	Tumor necrosis factor
VCAM1	Vascular cell adhesion molecule 1

Declarations

Ethics approval and consent to participate

The review board of the Ethical Committee of the Jessenius Faculty of Medicine CU approved the acquisition of human dental stem cells (approval No. EK 24/2020). Date of approval: 18 April 2020. Human third molars were obtained from healthy donors at the Department of Stomatology and Maxillofacial Surgery UHM. Informed consent was obtained from the patients/parents.

Consent for publication

Not applicable.

Availability of data and materials

All other datasets used in this study are available from the corresponding author upon reasonable request.

Competing interests

The authors declare no competing interests.

Fundings

This work was supported by VEGA 01/0104/26, GUKE 3183/2024. We gratefully acknowledge the financial support of the Ministry of Education, Research, Development, and Youth of the Slovak Republic (program EATRIS-SK) and the Integrated Infrastructure Operational Program for the project: Systemic public research infrastructure - Biobank for cancer and rare diseases, ITMS: 313011AFG5, co-financed by the European Regional Development Fund.

Author contributions

Conceptualization, B.B., and H.Š.; methodology, B.B., R.Z., T.P., B.G., V.K., N.Ž., S.N. and H.Š.; formal analysis B.B., R.Z., L.K. and H.Š.; investigation B.B., R.Z., T.P., B.G., V.K., D.D., N.Ž., and J.S.; validation M.K., S.N., M.J., J.S., E.H. and H.Š.; resources S.K., and R.J.; data curation B.B., R.Z., T.P., J.S. and H.Š, writing-original draft B.B., and H.Š.; writing-review and editing B.B., R.Z., M.K., J.S, Z.H., S.N. and H.Š.; visualization B.B., T.P., L.K. and H.Š.; supervision M.J., E.H. and H.Š.; project administration B.B., R.Z., and H.Š.; funding acquisition B.B., Z.H., S.N., E.H. and H.Š. All authors have read and approved the final version of the manuscript.

Acknowledgement

The authors thankful for Dr. Miroslava Šarlinová and Dr. Mária Škereňová for technical support. The authors declare that they have not use AI-generated work in this manuscript.

References

[1] Koushik TM, Miller CM, Antunes E. Bone tissue engineering scaffolds: function of multi-material hierarchically structured scaffolds. Adv Healthc Mater. 2023;12(9):e2202766. doi:10.1002/adhm.202202766.

[2] Li Y, Duan X, Chen Y, Liu B, Chen G. Dental stem cell-derived extracellular vesicles as promising therapeutic agents in the treatment of diseases. Int J Oral Sci. 2022;14(1):2. doi:10.1038/s41368-021-00152-2.

[3] Chen Y, Ma X, Mai H, Lai P, Huang R, Alimujiang A. The application of dental mesenchymal stem cells (DMSCs) in the repair of oral and maxillofacial defects. Front Bioeng Biotechnol. 2025;13:1677422. doi:10.3389/fbioe.2025.1677422.

[4] Inchingolo AM, Inchingolo AD, Nardelli P, Latini G, Trilli I, Ferrante L, Malcangi G, Palermo A, Inchingolo F, Dipalma G. Stem cells: present understanding and prospects for regenerative dentistry. J Funct Biomater. 2024;15(10):308. doi:10.3390/jfb15100308.

[5] Jin Z, Yang B, Zhang S, Liu Z, Wang Y, Lin A, Yang K, Yu M, Tian W, Huo F. Stem cell-driven biomedical technologies for tooth regeneration: engineering scaffolds, organoid models, and molecular targeted strategies. Stem Cell Res Ther. 2026. doi:10.1186/s13287-026-05044-y.

[6] Naz S, Khan FR, Khan I, Zohra RR, Salim A, Mohammed N, Ahmad T. Comparative analysis of dental pulp stem cells and stem cells from human exfoliated teeth in terms of growth kinetics, immunophenotype, self-renewal and multilineage differentiation potential for future perspective of calcified tissue regeneration. Pak J Med Sci. 2022;38(5):1228-1237. doi:10.12669/pjms.38.5.5187.

[7] Namjoynik A, Islam MA, Islam M. Evaluating the efficacy of human dental pulp stem cells and scaffold combination for bone regeneration in animal models: a systematic review and meta-analysis. Stem Cell Res Ther. 2023;14(1):132. doi:10.1186/s13287-023-03357-w.

[8] Wang L, Ruan M, Bu Q, Zhao C. Signaling pathways driving MSC osteogenesis: mechanisms, regulation, and translational applications. Int J Mol Sci. 2025;26(3):1311. doi:10.3390/ijms26031311.

[9] Huang W, Yang S, Shao J, Li YP. Signaling and transcriptional regulation in osteoblast commitment and differentiation. Front Biosci. 2007;12:3068-3092. doi:10.2741/2296.

[10] Lin X, Patil S, Gao YG, Qian A. The bone extracellular matrix in bone formation and regeneration. Front Pharmacol. 2020;11:757. doi:10.3389/fphar.2020.00757.

[11] Shiflett LA, Tiede-Lewis LM, Xie Y, Lu Y, Ray EC, Dallas SL. Collagen dynamics during the process of osteocyte embedding and mineralization. Front Cell Dev Biol. 2019;7:178. doi:10.3389/fcell.2019.00178.

[12] Pagani S, Salerno M, Filardo G, Locs J, van Osch GJVM, Vecstaudza J, Dolcini L, Borsari V, Fini M, Giavaresi G, Columbaro M. Human osteoblasts' response to biomaterials for subchondral bone regeneration in standard and aggressive environments. Int J Mol Sci. 2023;24(19):14764. doi:10.3390/ijms241914764.

[13] Pautke C, Schieker M, Tischer T, Kolk A, Neth P, Mutschler W, Milz S. Characterization of osteosarcoma cell lines MG-63, Saos-2 and U-2 OS in comparison to human osteoblasts. Anticancer Res. 2004;24(6):3743-3748. PMID:15736406.

[14] Baďurová B, Nystøl K, Michalič TO, Kucháriková V, Statelová D, Nováková S, Strnádel J, Halašová E, Škovierová H. Temporal profiling of cellular and molecular processes in osteodifferentiation of dental pulp stem cells. Biology (Basel). 2025;14(3):257. doi:10.3390/biology14030257.

[15] Okajcekova T, Strnadel J, Pokusa M, Zahumenska R, Janickova M, Halasova E, Skovierova H. A comparative in vitro analysis of the osteogenic potential of human dental pulp stem cells using various differentiation conditions. Int J Mol Sci. 2020;21(7):2280. doi:10.3390/ijms21072280.

[16] Shihan MH, Novo SG, Le Marchand SJ, Wang Y, Duncan MK. A simple method for quantitating confocal fluorescent images. Biochem Biophys Rep. 2021;25:100916. doi:10.1016/j.bbrep.2021.100916.

[17] Nováková S, Danchenko M, Okajčeková T, Baranovičová E, Kováč A, Grendár M, Beke G, Pálešová J, Strnádel J, Janíčková M, Halašová E, Škovierová H. Comparative proteomic and metabolomic analysis of human osteoblasts, differentiated from dental pulp stem cells, hinted crucial signaling pathways promoting osteogenesis. Int J Mol Sci. 2021;22(15):7908. doi:10.3390/ijms22157908.

[18] Kertys M, Grendar M, Kosutova P, Mokra D, Mokry J. Plasma based targeted metabolomic analysis reveals alterations of phosphatidylcholines and oxidative stress markers in guinea pig model of allergic asthma. Biochim Biophys Acta Mol Basis Dis. 2020;1866(1):165572. doi:10.1016/j.bbadis.2019.165572.

[19] Zahumenska R, Kalman M, Marcinek J, Mersakova S, Kertys M, Pindura M, et al. Establishment of PANDA - a new human pancreatic ductal adenocarcinoma cell line with 3D cell culture technology. Neoplasma. 2022;69(1):165-73. doi:10.4149/neo_2021_210924N1360.

[20] Hatoková Z, Baďurová B, Kertys M, Žideková N, Evinová A, Kotúľová L, Grendár M, Harvanová D, Slovinská L, Halašová E, Škovierová H, Nováková S. Biological and metabolomic characterization of human dermal fibroblasts and mesenchymal stem cells derived from human dental pulp and adipose tissue: a pilot comparative study. Stem Cell Rev Rep. 2025;21(8):2727-2744. doi:10.1007/s12015-025-10970-0.

[21] R Core Team. R: A language and environment for statistical computing. Version 4.5.3. Vienna (Austria): R Foundation for Statistical Computing; 2026. Available from: https://www.R-project.org/

[22] Wickham H. ggplot2: Elegant Graphics for Data Analysis. New York (NY): Springer-Verlag; 2016. doi:10.1007/978-3-319-24277-4.

[23] Kassambara A. ggpubr: 'ggplot2' Based Publication Ready Plots. R package version 0.6.3. Vienna (Austria): Comprehensive R Archive Network (CRAN); 2026. Available from: https://CRAN.R-project.org/package=ggpubr

[24] Rodríguez-Merchán EC. Bone healing materials in the treatment of recalcitrant nonunions and bone defects. Int J Mol Sci. 2022;23(6):3352. doi:10.3390/ijms23063352.

[25] Zha K, Tian Y, Panayi AC, Mi B, Liu G. Recent advances in enhancement strategies for osteogenic differentiation of mesenchymal stem cells in bone tissue engineering. Front Cell Dev Biol. 2022;10:824812. doi:10.3389/fcell.2022.824812.

[26] Kotova AV, Lobov AA, Dombrovskaya JA, Sannikova VY, Ryumina NA, Klausen P, Shavarda AL, Malashicheva AB, Enukashvily NI. Comparative analysis of dental pulp and periodontal stem cells: differences in morphology, functionality, osteogenic differentiation and proteome. Biomedicines. 2021;9(11):1606. doi:10.3390/biomedicines9111606.

[27] Kunimatsu R, Nakajima K, Awada T, Tsuka Y, Abe T, Ando K, Hiraki T, Kimura A, Tanimoto K. Comparative characterization of stem cells from human exfoliated deciduous teeth, dental pulp, and bone marrow-derived mesenchymal stem cells. Biochem Biophys Res Commun. 2018;501(1):193-198. doi:10.1016/j.bbrc.2018.04.213.

[28] Carluccio M, Ziberi S, Zuccarini M, Giuliani P, Caciagli F, Di Iorio P, Ciccarelli R. Adult mesenchymal stem cells: is there a role for purine receptors in their osteogenic differentiation? Purinergic Signal. 2020;16(3):263-287. doi:10.1007/s11302-020-09703-4.

[29] Sabbagh J, Ghassibe-Sabbagh M, Fayyad-Kazan M, Al-Nemer F, Fahed JC, Berberi A, Badran B. Differences in osteogenic and odontogenic differentiation potential of DPSCs and SHED. J Dent. 2020;101:103413. doi:10.1016/j.jdent.2020.103413.

[30] Cao Y, Boss AL, Bolam SM, Munro JT, Crawford H, Dalbeth N, Poulsen RC, Matthews BG. In vitro cell surface marker expression on mesenchymal stem cell cultures does not reflect their ex vivo phenotype. Stem Cell Rev Rep. 2024;20(6):1656-1666. doi:10.1007/s12015-024-10743-1.

[31] Dominici M, Le Blanc K, Mueller I, Slaper-Cortenbach I, Marini F, Krause D, Deans R, Keating A, Prockop DJ, Horwitz E. Minimal criteria for defining multipotent mesenchymal stromal cells. The International Society for Cellular Therapy position statement. Cytotherapy. 2006;8(4):315-317. doi:10.1080/14653240600855905.

[32] Kimura K, Breitbach M, Schildberg FA, Hesse M, Fleischmann BK. Bone marrow CD73+ mesenchymal stem cells display increased stemness in vitro and promote fracture healing in vivo. Bone Rep. 2021;15:101133. doi:10.1016/j.bonr.2021.101133.

[33] Moraes DA, Sibov TT, Pavon LF, Alvim PQ, Bonadio RS, da Silva JR, Pic-Taylor A, Toledo OA, Marti LC, Azevedo RB, Oliveira DM. A reduction in CD90 (THY-1) expression results in increased differentiation of mesenchymal stromal cells. Stem Cell Res Ther. 2016;7(1):97. doi:10.1186/s13287-016-0359-3.

[34] Kim YJ, Yu JM, Joo HJ, Kim HK, Cho HH, Bae YC, Jung JS. Role of CD9 in proliferation and proangiogenic action of human adipose-derived mesenchymal stem cells. Pflugers Arch. 2007;455(2):283-296. doi:10.1007/s00424-007-0285-4.

[35] Kannan S, Ghosh J, Dhara SK. Osteogenic differentiation potential of porcine bone marrow mesenchymal stem cell subpopulations selected in different basal media. Biol Open. 2020;9(10):bio053280. doi:10.1242/bio.053280.

[36] Wang Z, Ren L, Li Z, Qiu Q, Wang H, Huang X, Ma D. Impact of different cell types on the osteogenic differentiation process of mesenchymal stem cells. Stem Cells Int. 2025;2025:5551222. doi:10.1155/sci/5551222.

[37] Deshpande S, James AW, Blough J, Donneys A, Wang SC, Cederna PS, Buchman SR, Levi B. Reconciling the effects of inflammatory cytokines on mesenchymal cell osteogenic differentiation. J Surg Res. 2013;185(1):278-85. doi:10.1016/j.jss.2013.06.063.

[38] Dai J, Xiang G, Li J, Zhang G, Yang G, Xiao L, Wang Y, Zhang H. FTO-mediated MMP1 m6A modification promotes osteogenic differentiation of bone marrow mesenchymal stem cells via the ERK pathway in congenital scoliosis. Sci Rep. 2025;15(1):27673. doi:10.1038/s41598-025-13044-w.

[39] Fang S, Li Y, Chen P. Osteogenic effect of bone marrow mesenchymal stem cell-derived exosomes on steroid-induced osteonecrosis of the femoral head. Drug Des Devel Ther. 2018;13:45-55. doi:10.2147/DDDT.S178698.

[40] Iaquinta MR, Torreggiani E, Mazziotta C, Ruffini A, Sprio S, Tampieri A, Tognon M, Martini F, Mazzoni E. In vitro osteoinductivity assay of hydroxylapatite scaffolds, obtained with biomorphic transformation processes, assessed using human adipose stem cell cultures. Int J Mol Sci. 2021;22(13):7092. doi:10.3390/ijms22137092.

[41] Soukup R, Gerner I, Mohr T, Gueltekin S, Grillari J, Jenner F. Mesenchymal stem cell conditioned medium modulates inflammation in tenocytes: complete conditioned medium has superior therapeutic efficacy than its extracellular vesicle fraction. Int J Mol Sci. 2023;24(13):10857. doi:10.3390/ijms241310857.

[42] Alekos NS, Moorer MC, Riddle RC. Dual effects of lipid metabolism on osteoblast function. Front Endocrinol (Lausanne). 2020;11:578194. doi:10.3389/fendo.2020.578194.

[43] Blair HC, Kalyvioti E, Papachristou NI, Tourkova IL, Syggelos SA, Deligianni D, Orkoula MG, Kontoyannis CG, Karavia EA, Kypreos KE, Papachristou DJ. Apolipoprotein A-1 regulates osteoblast and lipoblast precursor cells in mice. Lab Invest. 2016;96(7):763-772. doi:10.1038/labinvest.2016.51.

[44] Dalle Carbonare L, Cominacini M, Trabetti E, Bombieri C, Pessoa J, Romanelli MG, Valenti MT. The bone microenvironment: new insights into the role of stem cells and cell communication in bone regeneration. Stem Cell Res Ther. 2025;16(1):169. doi:10.1186/s13287-025-04288-4.

[45] Chen L, Shi K, Frary CE, Ditzel N, Hu H, Qiu W, Kassem M. Inhibiting actin depolymerization enhances osteoblast differentiation and bone formation in human stromal stem cells. Stem Cell Res. 2015;15(2):281-289. doi:10.1016/j.scr.2015.06.009.

[46] Bispo DSC, Jesus CSH, Correia M, Ferreira F, Bonifazio G, Goodfellow BJ, Oliveira MB, Mano JF, Gil AM. NMR metabolomics assessment of osteogenic differentiation of adipose-tissue-derived mesenchymal stem cells. J Proteome Res. 2022;21(3):654-670. doi:10.1021/acs.jproteome.1c00832.

[47] Bispo DSC, Graça ICR, Jesus CSH, Rodrigues JE, Correia MC, Atella S, Duarte IF, Goodfellow BJ, Oliveira MB, Mano JF, Gil AM. Metabolic markers detect early osteodifferentiation of mesenchymal stem cells from multiple donors. Stem Cell Res Ther. 2025;16(1):294. doi:10.1186/s13287-025-04419-x.

[48] Gorres KL, Raines RT. Prolyl 4-hydroxylase. Crit Rev Biochem Mol Biol. 2010;45(2):106-24. doi:10.3109/10409231003627991.

[49] Badawy AAB. Kynurenine pathway of tryptophan metabolism: regulatory and functional aspects. Int J Tryptophan Res. 2017;10:1178646917691938. doi:10.1177/1178646917691938.

[50] Pham HT, Ono M, Hara ES, Nguyen HTT, Dang AT, Do HT, Komori T, Tosa I, Hazehara-Kunitomo Y, Yoshioka Y, Oida Y, Akiyama K, Kuboki T. Tryptophan and kynurenine enhances the stemness and osteogenic differentiation of bone marrow-derived mesenchymal stromal cells in vitro and in vivo. Materials (Basel). 2021;14(1):208. doi:10.3390/ma14010208.

[51] Pierce JL, Roberts RL, Yu K, Kendall RK, Kaiser H, Davis C, Johnson MH, Hill WD, Isales CM, Bollag WB, McGee-Lawrence ME. Kynurenine suppresses osteoblastic cell energetics in vitro and osteoblast numbers in vivo. Exp Gerontol. 2020;130:110818. doi:10.1016/j.exger.2019.110818.

[52] Vidal C, Li W, Santner-Nanan B, Lim CK, Guillemin GJ, Ball HJ, Hunt NH, Nanan R, Duque G. The kynurenine pathway of tryptophan degradation is activated during osteoblastogenesis. Stem Cells. 2015;33(1):111-121. doi:10.1002/stem.1836.

[53] Xiang T, Yang C, Xie L, Xiao S, Tang Y, Huang G, Sun D, Chen Y, Luo F. Aberrant tryptophan metabolism manipulates osteochondral homeostasis. Research (Wash D C). 2025;8:0728. doi:10.34133/research.0728.

[54] Qi T, Li L, Weidong T. The role of sphingolipid metabolism in bone remodeling. Front Cell Dev Biol. 2021;9:752540. doi:10.3389/fcell.2021.752540.

Supplementary Files

This is a list of supplementary files associated with this preprint. Click to download.

- SUMMARYdata.xlsx
- ReportMetabolomicprofillingQCsamplesBiocratesp180.xlsx
- BadurovaSupplementaryData.docx
- BadurovaSupplementaryDatarevised.docx